

MASSIVE STAR FORMATION IN OVERDENSE REGIONS OF THE EARLY UNIVERSE

JOHN A. REGAN*

Centre for Astrophysics and Space Science Maynooth, Department of Theoretical Physics, Maynooth University, Maynooth, Ireland
 Version April 27, 2023

ABSTRACT

Both the origin of, and the population demographics of, massive black holes (MBHs) remains an open question in modern day astrophysics. Here we introduce the **BlackDemon** suite of cosmological simulations using the **Enzo** code. The suite consists primarily of three, high resolution, distinct regions, each with a side length of $1 h^{-1}$ Mpc. Two of the regions evolve within a larger overdense region while the other evolves within a more ‘normal’ region. The simulation suite has spatial and mass resolution capable of resolving the formation of the first galaxies and MBHs within each region. We report here, as the first in a series of papers, the evolution of the simulation suite up to the point where star formation has commenced in each region and for 2 Myr after the onset of star formation. Within these environments the masses of the first objects to form have masses between approximately $100 M_{\odot}$ and $10^4 M_{\odot}$. The larger mass objects form due to both major mergers, which trigger rapid mass inflow to the centre of the halo, and also through multiple minor mergers which allows the host halo to grow to close to the atomic cooling threshold. In both scenarios the initially very high accretion rates quickly grow the objects to close to $10^4 M_{\odot}$. However, accretion halts after less than 50,000 years due to gas starvation. The final fate of these objects in terms of fragmentation and subsequent fragment mergers cannot be deduced at our current resolution. In the case where fragmentation is mild such objects are likely to form super-massive stars before contracting to the main sequence evolving into massive population III stars and subsequently MBHs.

Keywords: Early Universe, Supermassive Stars, Star Formation, First Galaxies, Numerical Methods

1. INTRODUCTION

Super-Massive Black Holes (SMBHs) with masses in excess of $10^6 M_{\odot}$ exist at the centre of most massive galaxies (Kormendy & Ho 2013). Moreover, high- z observations of distant quasars confirm that SMBHs with masses up to $10^9 M_{\odot}$ are in place less than one billion years after the Big Bang (e.g. Fan et al. 2006; Venemans et al. 2015; Matsuoka et al. 2019; Wang et al. 2021). Below the supermassive mass scale at masses between approximately 10^3 and $10^6 M_{\odot}$ there is speculated to exist a second population of massive black holes¹ - sometimes dubbed *intermediate mass black holes*. This intermediate mass range is key to understanding the astrophysical evolution of the entire MBH population.

Below this mass scale exist the stellar mass black holes - detectable in the local universe via both electromagnetic observations (e.g. Done, Gierliński & Kubota 2007) and through gravitational wave emission (e.g. Abbott et al. 2016). Stellar mass black holes are abundant in the local universe (and presumably across the entire universe) as they originate from the end-point of massive stars. The intermediate range of MBHs ($10^{3-6} M_{\odot}$) have proven very challenging to detect. This is because the accretion rate onto a black hole scales linearly with the mass of the black hole according to the Eddington formulation:

$$\dot{M}_{\text{MBH}} = \frac{4\pi G M_{\text{MBH}} m_{\text{p}}}{\epsilon \sigma_{\text{T}} c} \quad (1)$$

*E-mail: john.regan@mu.ie, Royal Society - SFI University Research Fellow

¹ I will use the generic term massive black holes to describe all black holes masses in excess of $10^3 M_{\odot}$ in this paper

where M_{MBH} is the black hole mass, m_{p} is the proton mass, ϵ is the radiative efficiency, σ_{T} is the Thomson cross section and c is the speed of light. Lower mass black holes therefore accrete at significantly lower rates compared to their more massive counterparts. The luminosity that is detectable from these intermediate sources is therefore lower as well making their overall detection more challenging with current instruments. Related to this is the fact that many of these intermediate mass black holes may not necessarily reside at the galactic centre and may instead be located at off-nuclear locations again increasing the challenge (Bellovary et al. 2010; Chiou et al. 2018; Reines et al. 2020; Druschke et al. 2020; Beckmann et al. 2022). Nonetheless, over the past decade significant progress has been made in detecting black holes with masses below $10^6 M_{\odot}$ (e.g. Baldassare et al. 2020).

In any case understanding the origin of all black holes within the MBH mass window is paramount. A key challenge is then to understand what the seed masses of the MBH mass spectrum are. Does the entire MBH mass spectrum originate from stellar mass black holes with characteristic masses of approximately $40 M_{\odot}$ which grow through accretion and mergers? Or is another channel required to populate the MBH mass spectrum? The simplest case is to assume that the seeds are ‘light’ and that they originated from the remnants of the first stars (e.g. Madau & Rees 2001). While this is indeed the simplest explanation there are significant challenges in growing these light seeds in order to explain the entire MBH mass spectrum. The problem is particularly acute when attempting to use light seed growth to explain the appearance of SMBHs at $z \gtrsim 7$. In order to achieve such growth the seed black holes would need to

grow, uninterrupted at the Eddington rate. Such a scenario has been shown to be exceedingly unlikely with numerous cosmological simulations showing that light seeds do not grow efficiently and tend to remain at their seed masses across cosmic time (Alvarez, Wise & Abel 2009; Milosavljević, Couch & Bromm 2009; Smith et al. 2018; Spinoso et al. 2022). Although see Zubovas & King (2021) who argue that, though unlikely and rare, episodes of chaotic accretion may result in the growth of light seeds to SMBH masses. Another possible avenue that may circumvent this growth hurdle (and may also apply to heavier seeds) is the super-Eddington accretion scenario (e.g. Sądowski 2009; Sądowski et al. 2014; Jiang, Stone & Davis 2017; Regan et al. 2019) and where, in some cases, if the gas inflow is sufficiently high a steady state can be reached without any time-dependent oscillations (Inayoshi, Haiman & Ostriker 2016a,b; Takeo, Inayoshi & Mineshige 2020). If the black hole can find itself at the centre of an extremely dense gas cloud then this mechanism may be viable and could in principle grow the embryonic black hole by several orders of magnitude in mass within a short timeframe.

Alternative routes to MBH formation may be through either a dynamical runaway or via the formation of a supermassive star. Both of these mechanisms create a “heavy” seed with masses in excess of approximately $10^3 M_{\odot}$. Numerous pathways to a MBH have been investigated via a dynamical pathway. Seminal work by Portegies Zwart et al. (2004) showed that MBHs can be formed through runaway collisions of stars in dense young star clusters. Additional research in this direction by other authors (Devecchi & Volonteri 2009; Katz, Sijacki & Haehnelt 2015; Rizzuto et al. 2021; González et al. 2021) has also shown that MBHs can form via this mechanism albeit it is challenging to grow black holes to masses greater than $10^3 M_{\odot}$ through this process. Related mechanisms where initial light seed black holes grow inside a nuclear star cluster (Alexander & Natarajan 2014; Lupi et al. 2014; Stone, Küpper & Ostriker 2017; Natarajan 2020; Fragione et al. 2022) or in other high density environments like a circumbinary disks (Lupi et al. 2016) offer additional, promising, routes to MBHs.

In addition to the dynamical pathway heavy seeds can form via the formation of a very massive or supermassive star (SMS). SMSs are defined by their extremely high accretion rate onto the stellar surface ($\dot{M} \gtrsim 0.001 M_{\odot} \text{ yr}^{-1}$) which, through the accretion of high entropy gas, causes the photosphere of the star to expand (so long as the accretion rate is maintained) (Haemmerlé et al. 2018b). Such stars are expected to the very red, in contrast to massive PopIII stars whose spectrum would be blue, and cool with effective temperatures of approximately $T_{\text{eff}} \sim 5000 \text{ K}$ (Hosokawa, Omukai & Yorke 2013; Hosokawa et al. 2013; Haemmerlé et al. 2018b; Woods et al. 2021). With maximum masses of greater than $10^5 M_{\odot}$ (Woods et al. 2017) these SMS stars would be ideal progenitors for MBHs. Over the last decade many groups have attempted to model the formation of SMSs in the first atomic cooling haloes. Atomic cooling haloes are believed to be necessary for SMS formation as the mass inflow rate scales with the mass of the host halo.

The formation of a SMS additionally requires metal-free (or near metal-free) gas and so previous genera-

tions of star formation in the halo (or the halo progenitors must be avoided). Strong, local sources of Lyman-Werner (LW) radiation can dissociate H_2 thus preventing or delaying the normal formation of PopIII stars (Machacek, Bryan & Abel 2001; Haiman 2006; Shang, Bryan & Haiman 2010; Wolcott-Green, Haiman & Bryan 2011; Visbal, Haiman & Bryan 2014a; Visbal et al. 2014; Visbal, Haiman & Bryan 2014b; Regan et al. 2017; Wolcott-Green & Haiman 2019; Skinner & Wise 2020; Schauer et al. 2021; Kulkarni, Visbal & Bryan 2021). However, the required flux from LW radiation has been shown to be large (Regan, Johansson & Haehnelt 2014; Latif et al. 2014b,a; Regan & Downes 2018b) and metal pollution from nearby haloes must also be avoided (Agarwal et al. 2017) meaning that the LW channel may be difficult to achieve in practice and may only be able to seed a subset of SMBHs. Finally, LW escape fractions may also be impeded from escaping early galaxies thus further reducing the effectiveness of this channel (Kitayama et al. 2004; Schauer et al. 2015, 2017).

Baryonic streaming velocities (Tseliakhovich & Hirata 2010) and the impact they have on halo formation has also been investigated as a potential channel for heavy seed MBH seed formation. In this case the extra kinetic energy in the gas, relative to the dark matter, delays the virialisation of the halo and therefore allows more massive haloes to develop before star formation can be achieved. Similar to the LW pathway this can lead to ideal environmental conditions for MBH seed formation to take place via SMS formation (Tanaka & Li 2014; Latif, Niemeyer & Schleicher 2014; Hirano et al. 2017; Schauer et al. 2017). Whether this channel can seed all MBHs is unclear but it may be possible to seed the massive end of the MBH mass spectrum in this way (Kulkarni, Visbal & Bryan 2021). Finally, the rapid assembly of haloes has also been shown to allow for SMS formation (Wise et al. 2019). In this case a halo grows at a sufficient rate that radiative cooling, due to H_2 emission lines, cannot overcome the dynamical heating effect of the rapid assembly (Yoshida et al. 2003; Fernandez et al. 2014). In this case the halo continues to grow without forming stars until either the growth rate slows or the halo begins cooling via atomic line emission cooling (Wise et al. 2019). The rapid assembly scenario has the advantage that it may produce a higher number density of MBH seeds (Regan et al. 2020a; Lupi, Haiman & Volonteri 2021) compared to either the LW pathway or the baryonic streaming pathway but it is still unclear whether very high final masses can be achieved for the seeds (Regan et al. 2020b; Latif et al. 2022). The goal of this simulation suite is to probe the different pathways, with the exception of the streaming velocities pathway, as self-consistently as possible. The rapid assembly process is captured due to the overdense nature of the environment with light seeds forming organically and captured via our star formation prescriptions. The LW pathway will be captured if such a condition can arise in our volume. The capture of dynamical pathways (i.e. the formation of nuclear stellar clusters) is also possible to capture as well but would require zoom-in re-simulations to probe in detail.

The paper is laid out as follows: In §2 we describe the methods used in designing and running the simulations and the rationale behind them. In §3 we analyse the re-

sults of the simulations up to the point where they are now. In §5 we summarize our results and outline our conclusions.

2. METHODS

2.1. *BlackDemon Simulation Suite*

The **BlackDemon** (Black Hole Demographics) simulation suite is a set of cosmological zoom-in simulations targeting the progenitor haloes of a massive halo ($M_{halo} \sim 6 \times 10^{11} M_{\odot}$ at $z = 6$) in an overdense region of the early Universe ($z > 15$) (see Figure 1). The **BlackDemon** simulations are run using the **Enzo** code (Bryan et al. 2014; Brummel-Smith et al. 2019) with a three stage setup required in order to achieve the mass resolution necessary to properly resolve the progenitor haloes of massive star and black hole formation.

Enzo has been extensively used to study the formation of structure in the early universe (Abel, Bryan & Norman 2002; O’Shea et al. 2005; Turk et al. 2012; Wise et al. 2012, 2014, 2019; Regan et al. 2020a). **Enzo** includes a ray tracing scheme to follow the propagation of radiation from star formation and black hole formation (Wise & Abel 2011) as well as a detailed multi-species chemistry model that tracks the formation and evolution of nine primordial species (Anninos et al. 1997; Abel et al. 1997). In particular the photo-dissociation of H_2 is followed, which is a critical ingredient for determining the formation of the first metal-free stars (Abel, Bryan & Norman 2000). The simulation suite uses a Planck-like (Planck Collaboration et al. 2014, 2020) cosmology with the following parameters $\Omega_M = 0.2592$, $\Omega_{\Lambda} = 0.7408$, $\Omega_b = 0.0487$, $H_0 = 67.7$, $\sigma_8 = 0.8159$ and $n = 0.9667$.

2.2. *Rationale*

The rationale guiding this simulation suite is to maximise resolution (both mass and spatial) within a highly overdense region of the early Universe. The goal is to investigate both galaxy and black hole formation in such a region. It is within these unusually overdense regions that the seeds of MBHs may be expected to form more readily (Regan et al. 2020a,b; Lupi, Haiman & Volonteri 2021; Latif et al. 2022; Chiaki et al. 2023). While there is significant theoretical evidence to back this up observational evidence is still uncertain regarding the high- z quasars at least (Willott et al. 2005; Kim et al. 2009; Simpson et al. 2014; Mazzucchelli et al. 2017) but see Overzier (2022) for tentative evidence for an overdensity near a high- z quasar. The simulation suite consists of three stages. Stage one involved running a low resolution dark matter only simulation to identify the Lagrangian region of a massive halo at high redshift. In stage two, nested grids were used to gain higher mass resolution in the region surrounding the massive halo identified in stage one. Individual haloes hosting early star formation were identified and then additional nested grids were added for the final stage three simulations. For each of stage one, stage two and stage three the entire $100 h^{-1}$ Mpc box is evolved. What changes from one stage to another is the positioning and extent of the nested grids. For stage two the extent of the most refined nested grid is $10 h^{-1}$ Mpc, for stage three the most refined nested

grid is $1 h^{-1}$ Mpc. All stages are initialised at $z = 100$.

We therefore initially identified a massive dark matter halo within a $100 h^{-1}$ Mpc volume, and by successively tracing back its progenitor haloes, investigated star and black hole formation in that environment. The region surrounding the formation of a massive halo is likely to experience far more mergers than a typical region and as such is the ideal laboratory to investigate the potentially complementary effects of both a rapid assembly history (Yoshida et al. 2003; Fernandez et al. 2014; Wise et al. 2019) including turbulent flows (Latif et al. 2022) and LW radiation (Haiman 2006; Shang, Bryan & Haiman 2010) - all of which have been advocated as mechanisms for forming SMSs and/or MBHs.

2.3. *The Stage One and Stage Two Simulations*

As already noted the zoom-in regions were chosen as part of a three stage process. Stage 1 involved running a large, low resolution, dark matter only simulation to find a massive dark matter halo in the early Universe. The initial conditions for this simulation were generated with MUSIC (Hahn & Abel 2011) within a $100 h^{-1}$ Mpc box run on a 2048^3 grid. This led to a particle resolution of $M_{part} \sim 8 \times 10^6 h^{-1} M_{\odot}$ with a spatial resolution of approximately $5 h^{-1}$ kpc (using 4 levels of adaptive refinement). The simulation was evolved to a redshift of $z = 6$. At this point the **Rockstar** halo finder (Behroozi, Wechsler & Wu 2013) was used to locate massive haloes within the box. Rather than simply choosing the most massive halo in the box we choose instead the halo with the lowest tidal field (e.g. Di Matteo et al. 2017) among the ten most massive haloes. Our selected halo had a mass of $M_{halo} \sim 6.1 \times 10^{11} M_{\odot}$ at $z = 6$ and a mass of $M_{halo} \sim 3 \times 10^{10} M_{\odot}$ at $z = 12$. This halo corresponds to a greater than 4σ fluctuation in the primordial density field.

Having found the massive halo we used this to centre our next simulation and placed six static nested grids around the halo. The finest grid was $10 h^{-1}$ Mpc on the side and gave a maximum particle resolution of $M_{part} \sim 10^5 h^{-1} M_{\odot}$. This stage 2 simulation was run with full baryonic physics turned on including the star formation prescription described in §2.5. No feedback was employed in this stage however. The goal of this stage was simply to identify the clustered regions inside this sub-volume within which (massive) star formation initially takes place. At this particle mass resolution only haloes with masses of a few times $10^6 M_{\odot}$ could be resolved and so while this simulation cannot determine the true pathways to early star formation it nonetheless provided us with the information we need to continue to stage 3. The stage 2 simulations were evolved to $z = 17.9$.²

At $z = 17.9$ we had 31 haloes undergoing active star formation inside this $10 h^{-1}$ Mpc sub-region ($\sim 0.5 h^{-1}$ Mpc physical). This allowed us to identify three distinct “clusters” of star formation (see Figure 1). These three clusters provided us with the initial conditions required to begin our stage 3 simulations. For stage 3 an additional two static nested grids (so eight in total) were

² We terminated the simulations at this point as our initial goal is to run the Stage 3 simulations to $z = 18$.

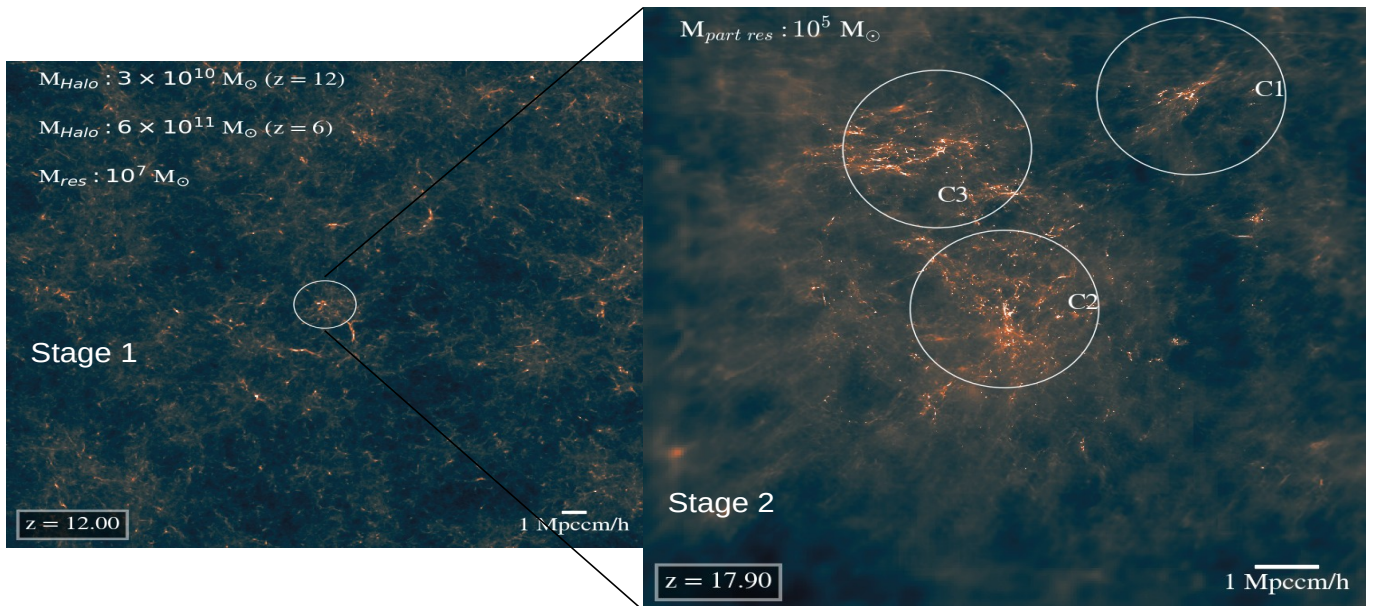


Figure 1. The initial setup required to identify the clusters needed to run our stage 3 simulations. In stage 1 (left hand side) a dark matter only simulation is evolved to a redshift of 6 in a box of side length $100 h^{-1}$ Mpc. Within this large box the most massive halo with the lowest tidal field is identified (white circle). The halo has a mass of $M_{halo} = 3 \times 10^{10} M_{\odot}$ at $z = 12$ and $M_{halo} = 6 \times 10^{11} M_{\odot}$ at $z = 6$. Halos are identified and their mass determined using the **Rockstar** halo finder (Behroozi, Wechsler & Wu 2013). For stage 2 we re-centre our initial conditions over this halo and rerun the simulations including baryonic physics, a 9 species chemical model and star formation in order to identify clusters of star formation in a $10^3 h^{-3} \text{ Mpc}^3$ volume surrounding the halo found in stage 1. Three clusters are identified - as shown on the right hand side. For stage 3 we construct initial conditions surrounding each cluster with each cluster having a (comoving) volume of $1^3 h^{-3} \text{ Mpc}^3$. The clusters do not overlap as can be seen in the figure. The separation from the centre of one region to the centre of another varies from a minimum separation of 3.3 comoving Mpc/h to a maximum separation of 5.5 comoving Mpc/h. In total 31 haloes were observed to experience star formation during stage 2. The maximum mass resolution in Stage 1 is $M_{res} = 10^7 M_{\odot}$, while in Stage 2 the maximum mass resolution is $M_{res} = 10^5 M_{\odot}$. In stage 3 the maximum mass resolution is $M_{res} \sim 2.3 \times 10^3 M_{\odot}$.

placed around each cluster. This gives three different initial conditions each centred on a different cluster (named Cluster1, Cluster2 & Cluster3). Additionally, we created initial conditions for a $1 h^{-1}$ Mpc “ControlRegion” which is not connected to the overdense region in any way and was instead selected from a region of cosmic mean density chosen randomly from the parent box. The “ControlRegion” is run under a setup identical to the cluster regions and acts as a control to compare against the results from the overdense region. Within the finest static mesh encompassing each cluster (including the “ControlRegion”) the maximum particle resolution is now $M_{part} \sim 2.3 \times 10^3 M_{\odot}$. Each region has a side length of $1 h^{-1}$ Mpc³. Within this region adaptive mesh refinement is permitted down to a maximum depth of 20. This corresponds to a maximal spatial resolution of $\Delta x \sim 0.05$ pc (physical, 1.1 pc (comoving)) at $z = 20$.

2.4. Stage 3 simulations

The stage 3 simulations, which are currently still running, are designed to be able to resolve all of the pathways to MBH formation as self-consistently as possible. The refinement criteria used here are based on three physical measurements: (1) The dark matter particle over-density, (2) the baryon over-density and (3) the Jeans length. The first two criteria introduce additional meshes when the over-density ($\frac{\Delta \rho}{\rho_{\text{mean}}}$) of a grid cell with respect to the mean density exceeds 8.0 for baryons

³ We initially tried larger high resolution volumes but they proved intractable

and/or DM. Furthermore, we set the *MinimumMassForRefinementExponent* parameter to -0.1 making the simulation super-Lagrangian and therefore reducing the threshold for refinement as higher densities are reached. For the final criteria we set the number of cells per Jeans length to be 4 in these runs.

The stage 3 simulations require our full physics model implementation to accurately track massive star and black hole formation as well as accretion and feedback. Our particle resolution of $M_{part} \sim 2.3 \times 10^3 M_{\odot}$ allows us to identify all haloes with masses above approximately $10^5 M_{\odot}$. The minimal Jeans mass for gravitational collapse is expected to be above this threshold mass (Bryan & Norman 1998; Fuller & Couchman 2000; Machacek, Bryan & Abel 2001; Yoshida et al. 2003; Skinner & Wise 2020; Schauer et al. 2021; Kulkarni, Visbal & Bryan 2021) meaning that these simulations are capable of resolving the first mini-haloes. The focus on an overdense region means that these clusters and the individual haloes within them are very likely to be subject to dynamical heating from repeated minor mergers (Yoshida et al. 2003; Fernandez et al. 2014; Wise et al. 2019), turbulent flows (Latif et al. 2022) as well as merger triggered star formation (Hopkins et al. 2013) all of which have been shown to drive massive star formation in haloes which are already above the threshold for gravitational collapse. The stage 3 simulation suite include a full multi-species model including a primordial chemical network of 9 species with the detailed chemical network solved using the **Grackle-2.1** library (Smith et al. 2017). **Grackle-2.1** models self-shielding of H_2 us-

ing the prescription given by [Wolcott-Green, Haiman & Bryan \(2011\)](#), shielding of H_2 due to intervening neutral Hydrogen is currently not part of `Grackle-2.1` and could be added in the future to improve the accuracy of modelling H_2 abundances (e.g. [Schauer et al. 2015](#)). Star formation is tracked self-consistently and is detailed below.

2.5. Subgrid Star Formation & Black Hole Prescription

In order to resolve star formation in the collapsing target haloes we set the maximum refinement level of the stage 3 simulations to 20 which corresponds to a maximum spatial resolution of $\Delta x \sim 0.05$ pc at $z = 20$.

To model star formation within the collapsing gas cloud we employed a star formation criteria using the methodology first described in [Krumholz, McKee & Klein \(2004\)](#) and more recently in [Regan & Downes \(2018a,b\)](#); [Regan et al. \(2020b\)](#). Stars are formed when all of the following conditions are met:

1. The cell is at the highest refinement level
2. The cell exceeds the Jeans density
3. The flow around the cell is converging
4. The cooling time of the cell is less than the freefall time
5. The cell is at a local minimum of the gravitational potential

The simulation results reported here are at the point where initial gravitational collapse has been attained in all four regions and star formation and evolution is subsequently tracked in the ControlRegion, Cluster2 and Cluster3. While we track the initial evolution of four separate regions we only track the onset of star and black hole formation in the ControlRegion, Cluster2 and Cluster3 due to the computational expense of the simulations. Within the three regions in which we track star formation three of the first five stars to have formed have collapsed into MBHs.

In tracking star formation in such an overdense environment the question becomes what type of star is formed at the outset of star formation and how does that star evolve over time? The type of star that forms is based on the following logical sequence:

1. If the (gas-phase) metallicity⁴ is greater than $10^{-4} Z_\odot$ then a cluster of PopII stars is formed (represented by a single particle)
2. If the metallicity is less than $10^{-4} Z_\odot$ and the accretion rate onto the cell is greater than $0.01 M_\odot \text{ yr}^{-1}$ then a SMS forms (note that for initial formation we require an accretion rate a factor of ten above the critical accretion rate⁵ to ensure we are well inside the accretion rates necessary for SMS formation)

⁴ Note that all metallicities referred to in this paper are gas phase metallicities.

⁵ we take the critical accretion rate for SMSs to be $0.001 M_\odot \text{ yr}^{-1}$ ([Haemmerlé et al. 2018b](#))

3. If the metallicity is less than $10^{-4} Z_\odot$ and the accretion rate onto the cell is less than $0.01 M_\odot \text{ yr}^{-1}$ and the H_2 fraction is greater than 5×10^{-4} then a PopIII star forms
4. Otherwise no star particle is created and the code continues to check for star formation regions

The initial masses assigned to stars are determined by their type. SMSs accrete material and hence their masses are calculated self-consistently. PopII and PopIII stars have initial masses assigned at birth. All PopII (clusters) are assigned masses based on the overdensity in the cell, compared to the Jeans density. The minimum PopII mass is set to be $10^3 M_\odot$. Pop II star particles represent a star cluster of some total mass and an assumed normal (Gaussian) IMF. To generate the PopII star particles a sphere is created around the maximum density cell and a fraction $c_* = 0.07 \times f_{\text{cold}}$ of the cold gas, f_{cold} , is converted into stars (with a minimum cluster mass of $1000 M_\odot$). PopIII stars on the otherhand have initial masses assigned according to the same process as used in the *Renaissance* suite of simulations (e.g [Chen et al. 2014](#)). In this case masses are chosen randomly from an initial mass function with a functional form given by

$$f(\log M)dM = M^{-1.3} \exp\left[-\left(\frac{M_{\text{char}}}{M}\right)\right]dM \quad (2)$$

This form behaves as a power-law at $M > M_{\text{char}}$ and is exponentially cutoff below that mass ([Chabrier 2003](#)). We choose $M_{\text{char}} = 40 M_\odot$ consistent with recent result of PopIII formation simulations in the literature ([Turk, Abel & O’Shea 2009](#); [Clark et al. 2011](#); [Stacy & Bromm 2014](#); [Hirano et al. 2014](#)). The PopIII mass range runs from $1 M_\odot$ up to $300 M_\odot$. The star formation criteria evoked here combined with our maximum spatial resolution results in a typical Jeans Density at the centre of the collapsing structures of a few times 10^6 cm^{-3} . It also needs to be emphasised that this density resolution is insufficient to probe the true spatial scale of star formation. In practice our results should therefore be interpreted in this light in the knowledge that subsequent fragmentation may reduce the masses of the individual stars. Although there is good reason to believe that the regions modelled here, which experience high gas inflows, form very massive central objects even in the face of fragmentation (e.g. [Reinoso et al. 2023](#)). Black holes, when formed, form with the same mass as the progenitor star.

Subsequent to a star forming and being assigned a type, accretion onto the star is tracked if the star is either a SMS or a black hole. We do not have sufficient resolution in these simulations to track accretion onto PopIII stars (which are much more compact than SMSs). PopII clusters also do not accrete. As discussed in the Introduction SMSs are stars with low surface temperatures that are appropriate for main sequence SMSs and less massive proto-stars on the Hayashi track. Rapidly accreting (i.e. $\dot{M}_* \gtrsim 0.001 M_\odot/\text{yr}$) protostars carry large amounts of entropy (hot accretion) into the stellar interior. The stellar radius monotonically increases as the stellar mass increases obeying an analytic mass-radius relation ([Hosokawa, Yorke & Omukai 2010](#); [Hosokawa, Omukai & Yorke 2013](#); [Hosokawa et al. 2013](#)).

Cluster Name	Current Redshift	First Star Formation Redshift	# Haloes ($M_{Halo} \geq 1 \times 10^5 M_{\odot}$)	Maximum Halo Mass [M_{\odot}]
Cluster1	22.28	-	1361	2.65×10^6
Cluster2	22.80	23.06	2826	1.72×10^7
Cluster3	22.10	22.31	3522	2.36×10^7
ControlRegion	19.8	20.00	321	1.81×10^6

Table 1

Cluster statistics at the current time of reporting. From left to right we have the cluster name, the current cluster redshift at the time of reporting, the redshift of first star formation in each cluster (note we do not follow Cluster1 to the point of star formation) the number of resolved haloes within the cluster region and the maximum halo mass in the region at the cluster redshift.

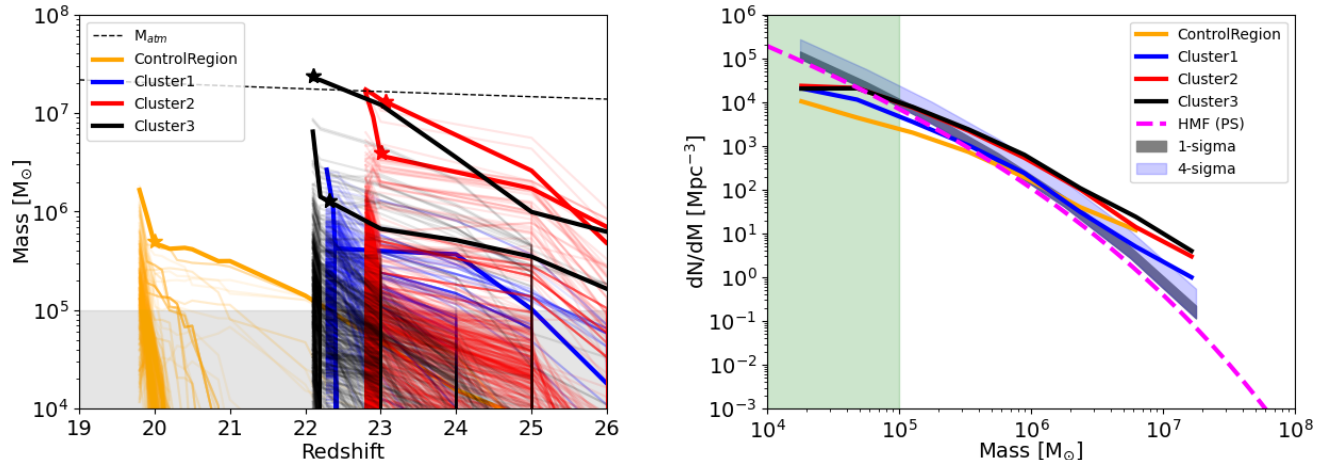


Figure 2. *Left Panel:* The growth of a large selection of haloes from each of Cluster1, Cluster2, Cluster3 and the ControlRegion. Each cluster is identified by colour - blue for Cluster1, red for Cluster2, green for Cluster3 and orange for the ControlRegion. The star forming haloes (or the first halo to undergo gravitational collapse in the case of Cluster1) are marked by the thick line and star markers indicating the redshift of first star formation. At the redshifts to which the simulations have now evolved most resolved haloes are between $10^5 M_{\odot}$ and $10^7 M_{\odot}$. *Right Panel:* The halo mass function from each of Cluster1, Cluster2, Cluster3 and the ControlRegion at the final output in each case. Overlaid on top (magenta dashed line) is the halo mass function from the publicly available HMF library (Murray, Power & Robotham 2013) as well as the 1-sigma and 4-sigma bands from the HMF computed halo mass function.

$$R_* \approx 2.6 \times 10^3 R_{\odot} \left(\frac{M_*}{100 M_{\odot}} \right)^{1/2} \quad (3)$$

where R_* is the stellar radius and M_* is the stellar mass. Note that the relation is independent of the actual accretion rate. The stellar interior remains inhomogeneous and subsequently contracts radiating energy away. A surface layer containing a small fraction of the mass inflates leading to a puffy SMS with low effective temperatures. The expansion continues until the radius eventually begins to contract when the mass of the star exceeds $M_* \gtrsim 3 \times 10^4 M_{\odot}$. This occurs because H^- bound-free opacity, which keeps the stellar surface temperature locked at close to 5000 K becomes unavailable as the density in the surface layer drops below $10^{-11} \text{ g cm}^{-3}$. Nonetheless, the radius at this stage of its evolution is approximately 100 AU. While this stellar radius is still below our resolution scale we nonetheless calculate the accretion rate flowing radially onto a region with a radius of 4 cell widths around the particle and use the accretion formalism of Krumholz, McKee & Klein (2004) to approximate the accretion rate onto the stellar surface for SMSs.

Assuming a star is designated as a SMS initially, as the simulation evolves the accretion rate onto a SMS can drop below the critical rate in which case the star contracts to the main sequence and becomes a PopIII

star. This reflects the contraction of the Pop III star to the main sequence on the Kelvin-Helmholtz timescale. For the simulation resolution of BlackDemon we do not have sufficient resolution to track accretion onto PopIII stars and hence once the star becomes a PopIII star (either at formation or as a result of transitioning from a SMS to a PopIII star) it will remain a PopIII star until the end of its stellar lifetime. Pop III stars are modelled assuming a blackbody spectrum with an effective temperature of $T_{eff} = 10^5 \text{ K}$ (Schaerer 2002) (no mass loss rates) while SMSs are modelled by assuming a blackbody spectrum with an effective temperature of $T_{eff} = 5500 \text{ K}$ (Hosokawa et al. 2013). The luminosity rates for the PopIII star as given by Schaefer (2002) have recently been verified by Haemmerlé et al. (2018a) who recover the rates of Schaefer (2002) for cases where the accretion rate is below the critical rate.

At the end of its stellar lifetime (for both SMSs and PopIII stars) the star transitions into a black hole particle and depending on its mass perhaps through the intermediate stage of a supernova explosion.

SMS always collapse directly to a black hole (Woods et al. 2017) with the black hole retaining the same mass as the final SMS mass. PopIII stars in the range $20 M_{\odot} < M_{PopIII} < 40.1 M_{\odot}$ undergo a type II supernova explosion and subsequently transition into a black hole. PopIII stars in the range $140 M_{\odot} < M_{PopIII} < 260 M_{\odot}$ undergo a pair instability explosion with no remnant

and the particle is removed from the simulation. PopIII stars in the range $40.1 M_{\odot} < M_{\text{PopIII}} < 140 M_{\odot}$ and those with masses in excess of $260 M_{\odot}$ directly collapse into black holes of the same mass.

2.6. Subgrid Feedback

The radiative feedback from the stellar population depends on the stellar type. We use mass-dependent infrared, Hydrogen ionizing, LW and Helium ionising luminosities and lifetimes of both the PopII and Pop III stars from [Schaerer \(2002\)](#). For PopIII stars the radiative feedback, which is propagated through the simulation using the in-built ray tracing formulation of [Wise & Abel \(2011\)](#), models the radiation in five radiation bins from the infrared, to LW, to Hydrogen ionising radiation to both singly Helium ionising and doubly Helium ionising radiation. The energies assigned to each radiation bin are taken from [Schaerer \(2002\)](#). In a similar vein the radiative feedback from metal enriched PopII stars is also taken from [Schaerer \(2002\)](#) with radiation in this case spread across four radiation bins from LW, to Hydrogen ionising, to single and doubly ionising Helium radiation. SMSs are modelled by assuming a blackbody spectrum with an effective temperature of $T_{\text{eff}} = 5500 \text{ K}$ ([Hosokawa et al. 2013](#)). The radiation spectrum for a SMS therefore peaks in the infrared as opposed to the UV for Pop III stars. For the specific luminosity of the SMS we take a characteristic mass of $500 M_{\odot}$ and apply the contribution from the non-ionising photons only ([Schaerer 2002](#)). The SMS luminosity changes as mass is accreted and the total luminosity then scales up as the mass increases. When SMSs stars transition into PopIII stars we continue to model the radiative feedback below the Hydrogen ionisation edge using ray tracing. To limit the computational challenges we do not model the ionising radiation. Instead the feedback is approximated using a thermal feedback model where the gas surrounding the star is heated to $T = 10^5 \text{ K}$ hence ionising all of the in-situ gas. This approximation is likely to be robust given that the ionising radiation is not expected to break out from the immediate vicinity of the star given the large column densities (e.g. [Woods et al. 2021](#); [Jaura et al. 2022](#)).

To model the radiative feedback from black hole particles we assume a multi-colour disk for the accretion disk and then a fit a corona with a power law (e.g. [Done et al. 2012](#)). We divide the energy radiated equally between the multi-colour disk and the power law component. For black holes we split the radiation into five energy bins from infrared up to hard X-rays. The energy bins used are 2.0 eV, 12.8 eV, 19.1eV, 217.3 eV and 5190 eV with the actual value of the luminosity at each timestep determined by the accretion rate at that timestep - if there is no accretion then there is no feedback. The fractional energy in each energy bin is then determined by the accretion rate onto the black hole and the mass of the black hole. We do not model kinetic or mechanical feedback from black holes in this suite of simulations.

3. RESULTS

This first paper in the **BlackDemon** (Black Hole Demographics) series examines the formation of dark matter

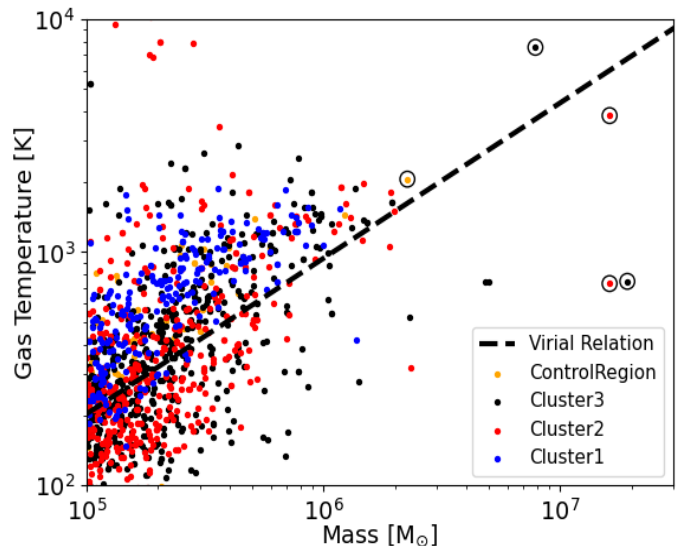


Figure 3. Halo mass as a function of gas temperature at the virial radius of each halo. Each cluster is coloured uniquely as described in the legend. Those haloes which have collapsed and are beginning to form stars are circled to allow for easy identification. The haloes, in general, follow a trend of increasing temperature with mass in this regime. The five star forming haloes from the ControlRegion, Cluster2 and Cluster3 are marked by the open circles. The star forming massive haloes have temperatures that are impacted by (stellar) feedback in some cases. We also show Eqn 5, as a dashed line, showing that the haloes follow very closely the expected virial relation i.e. $T_{\text{vir}} \propto M_{\text{halo}}^{2/3}$. We calculate the virial relation at $z = 20$.

haloes and embryonic galaxies in an overdense region. This analysis investigates early halo formation immediately prior to gravitational collapse which leads to the first star in each region and the subsequent evolution for more than two million years⁶. Galaxies in this overdense environment are predicted to be influenced by the rapid assembly of dark matter haloes in such an environment and as such may not necessarily follow, in all cases, the predictions from theory when the H_2 fraction is taken as the primary driver of catastrophic cooling and collapse. We begin by reviewing the relevant physical processes that are predicted to drive cooling in this regime and then compare these results to the results of our numerical simulations across each of our four regions (Cluster1, Cluster2, Cluster3 and the ControlRegion).

Table 1 outlines the current conditions in each region (i.e. at the point of gravitational collapse of the first halo in Cluster1 and approximately 2 Myr after the formation of the first star in each of the ControlRegion, Cluster2 and Cluster3). The table gives the number of resolved (at the current redshift) haloes in each cluster, the cluster redshift at the time of reporting, the redshift of first star formation and the maximum halo mass at this epoch in each case. The left panel of Figure 2 shows the mass

⁶ Beyond the formation for the first star in each clustered region we follow only the evolution of Cluster2 and Cluster3. This is because Cluster2 and Cluster3 show the highest abundance of rapidly growing haloes which is of most interest in this study. Additionally we follow the evolution of the ControlRegion for comparison.

of a selection of haloes against redshift⁷. Each Cluster is coloured uniquely (blue for Cluster1, red for Cluster2, black for Cluster3 and orange for the ControlRegion). The star forming haloes (or the first to undergo gravitational collapse in the case of Cluster1) are identified by thick lines, with star markers indicating the redshift of first star formation, in each case. What is immediately clear is that the regions in the overdense regions all have higher collapse masses compared to the ControlRegion. The most massive halo currently exists in Cluster3 and has a mass approximately an order of magnitude larger than that in the ControlRegion. The values below $M_{Halo} = 10^5 M_\odot$ are shaded as haloes below this scale are not well resolved in our simulations ($M_{part} \sim 2.3 \times 10^3$). Nonetheless, we show their growth history through this mass range for completeness.

To complement the mass growth plot in the right hand panel of Figure 2 we plot the halo mass function for each cluster. We additionally plot the halo mass function for a press-schechter mass function (Press & Schechter 1974) using the HMF library (Murray, Power & Robotham 2013) (magenta dashed line) as well as the 1-sigma and 4-sigma bands. Both Cluster2 and Cluster3 show significant deviations from the PS mass function reflective of the fact that they are rare manifestations of mean structure formation. The ControlRegion and Cluster1 align more closely with the PS mass function. Note that all four regions show deviations from the analytical fits at low ($\lesssim 2 \times 10^5 M_\odot$) and high ($\gtrsim 5 \times 10^6 M_\odot$) halo masses but this is due to poor statistics at these extremes. We will see again in §3.2 that Cluster2 and Cluster3 exhibit strong characteristics of evolving inside a highly overdense region.

3.1. Analytical Predictions

The first mini-haloes in our Universe are expected to form with masses greater than $10^6 M_\odot$ (Bryan & Norman 1998) with the cooling within these first small galaxies driven by the presence of H_2 (Tegmark et al. 1997). It is therefore instructive to consider how the predicted H_2 cooling timescale, τ_{H_2} , evolves. The timescale for H_2 cooling can be written as:

$$\tau_{H_2} = \frac{1}{\gamma - 1} \frac{n_{\text{gas}}}{n_{\text{H}}^2 f_{H_2}} \frac{k_B T_{\text{vir}}}{\Lambda_{H_2}} \quad (4)$$

where γ is the adiabatic constant, n_{gas} is the gas number density, k_B is the Boltzmann constant, T_{vir} is the halo virial temperature, n_{H} is the hydrogen number density, f_{H_2} is the H_2 fraction and $\Lambda_{H_2}(T)$ is the H_2 cooling function given by $\Lambda_{H_2}(T) = 10^{-27.6} (T_{\text{vir}}/100)^{3.4} \text{ erg s}^{-1} \text{ cm}^3$. This fitting is valid for temperatures in the range $120 \text{ K} \leq T \leq 6400 \text{ K}$ (Trenti, Stiavelli & Shull 2009). The virial temperature of a halo can be calculated analytically as

$$T_{\text{vir}} = \kappa \left(\frac{\mu}{0.6} \right) \left(\frac{\Omega_m}{\Omega_{mz}} \frac{\Delta_{\text{vir}}}{18\pi^2} \right)^{1/3} \left(\frac{h M_{\text{vir}}}{10^8 M_\odot} \right)^{2/3} \left(\frac{1+z}{10} \right) \quad (5)$$

⁷ subhaloes are largely excluded leaving only haloes with unique assembly histories

where $\kappa = 1.98 \times 10^4$, μ is the mean molecular weight, Ω_m is the cosmological matter density, $\Omega_{mz} = \frac{\Omega_m(1+z)^3}{\Omega_m(1+z)^3 + \Omega_\Lambda}$, $\Delta_{\text{vir}} = 18\pi^2 + 82d - 39d^2$, $d = \Omega_{mz} - 1$ and M_{vir} is the halo virial mass (Barkana & Loeb 2001; Lupi, Haiman & Volonteri 2021).

For each dark matter halo identified in our Stage 3 simulations (halos are identified using the Rockstar halo finder) we can calculate the H_2 cooling time for each halo since we have the required information (i.e. H_2 fraction, halo virial mass and virial temperature). Since our simulations have a full hydro component we also know the actual cooling time of the halo as calculated using Grack1e. We are therefore able to use the analytical predictions to directly compare against the full hydrodynamical results in order to observe the impact of local environmental conditions on gravitational collapse inside the first structures and compare them against analytic predictions.

As the hierarchical structure within a cosmological region develops, halos grow through a series of mergers. The frequency and magnitude of the merging process effects the ability of the gas to cool as kinetic energy is added to the gas via the dark matter build up. The energy injected as a result of this process can be referred to as ‘‘dynamical heating’’ and was initially investigated numerically by Yoshida et al. (2003). In their N-body/SPH simulations they found that haloes that exceeded a critical growth rate generated sufficient heating within a halo to offset H_2 cooling and hence delay gravitational collapse. The critical growth rate is given by

$$\left. \frac{dM}{dt} \right|_{\text{crit}} \approx \left(\frac{n_H}{10^2} \right) \left(\frac{M}{10^6 M_\odot} \right)^{1/3} \Lambda_{H_2} \left(\frac{T}{1000 \text{ K}} \right) \left(\frac{f_{H_2}}{10^{-4}} \right) \left(\frac{1}{\alpha_{\text{vir}} (T/1000 \text{ K}, M/10^6 M_\odot)} \right) \left(\frac{\gamma - 1}{k_B} \right) M_\odot/\text{yr} \quad (6)$$

where $\alpha_{\text{vir}} = T_{\text{vir}} / (M_{\text{vir}} / M_\odot)^{2/3}$ and n_H is the number density of Hydrogen at the virial radius. Using the canonical values above the critical halo growth rate is approximately

$$\left. \frac{dM}{dt} \right|_{\text{crit}} \approx 1 M_\odot/\text{yr} \quad (7)$$

3.2. Halo Characteristics within the Overdense Regions

We begin our quantitative analysis of the haloes by examining the halo mass - temperature plane of the haloes from our simulation clusters. In Figure 3 we show the halo mass against the halo temperature, haloes from different clusters are coloured as indicated in the legend (orange for the ControlRegion, blue for Cluster1, red for Cluster2 and black for Cluster3). The gas temperature is calculated by taking the density weighted average value at the halo virial radius. From Figure 3 we can see that the halos follow a trend of increasing temperature with mass as expected in this low mass (density) regime. The star forming haloes from the ControlRegion, Cluster2 and Cluster3 are marked by open circles and have virial temperatures of between a few hundred Kelvin up to almost 10^4 Kelvin. The higher temperatures seen in some of these massive, star forming, haloes is due to the impact of stellar feedback (see §4).

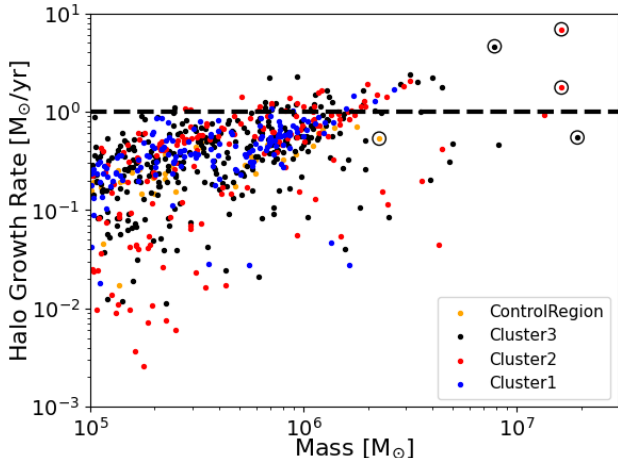


Figure 4. The growth rate of each halo plotted against its mass. Each cluster is distinguished by its colour as described in the legend. Only those haloes for which the calculated cooling time is less than a tenth of the Hubble time are shown. The growth rate shown is the instantaneous growth rate (i.e. the growth rate of each halo at this snapshot time). The star forming haloes (circled) in Cluster2 and Cluster3 all have relatively high growth rates. The star forming halo in the ControlRegion has a more modest growth rate but its halo mass is significantly lower and the halo resides in a more 'normal' environment.

In Figure 4 we plot the halo growth rate as a function of halo mass. Furthermore, we include only those haloes which have calculated cooling times (from Grackle) which are a factor of 10 shorter than the Hubble time at this redshift. We choose cooling times which are only a tenth of the Hubble time given the very early age of the Universe at this epoch and hence it's comparatively short age. Comparing to the full Hubble time at this epoch would be misleading and we use the, admittedly somewhat arbitrary, value of one tenth the Hubble value to be conservative.

The overall distribution shows a large scatter with values ranging from $10^{-3} M_{\odot} \text{ yr}^{-1}$ to greater than $1 M_{\odot} \text{ yr}^{-1}$. The dashed horizontal line shows the critical growth rate that must be achieved to drive dynamical heating which can offset cooling due to H_2 . The critical growth rate is for a halo of mass $10^6 M_{\odot}$, temperature, $T = 1000 \text{ K}$, and a H_2 fraction of $f_{\text{H}_2} = 10^{-4}$. A handful of haloes (predominantly from Cluster2 and Cluster3) show mass growth rates exceeding this critical value. Additionally, three of the five star forming haloes have growth rates significantly above the critical rates while also being in a regime where atomic cooling may not yet be fully active given the haloes relatively low temperatures. The halo growth rates in this case (i.e. dM/dt) is computed by calculating the finite difference in halo masses between the current and previous data output.

3.3. Determining the impact of dynamical heating

We now attempt to extract the effect of dynamical heating in such an overdense region. We begin by examining the predicted cooling time due to H_2 cooling on each halo and compare that against the actual cooling time for each halo. When retrieving the H_2 fractions and the (grackle calculated) cooling times from the simulation data all

quantities are extracted from the simulation within a 10 pc sphere centred on the densest point in the halo. Both the H_2 and cooling times are taken as density weighted averages. The timescale for H_2 cooling is given by Eqn 4. In Figure 5 we plot the predicted cooling time for each halo in grey. Over-plotted onto this we plot (colouring each region again) the calculated cooling time for each halo. Again we only plot the cooling times for haloes with cooling times shorter than one tenth of the Hubble time. There is substantial scatter at halo masses below $M_{\text{Halo}} = 5 \times 10^5 M_{\odot}$ and hence we only show haloes above this mass threshold.

Above $M_{\text{Halo}} = 10^6 M_{\odot}$ we can clearly discern the impact of rapid assembly. The grey points, which represent the analytical predictions for each halo based on the halo H_2 fraction systematically under-predict the gas cooling times (particularly for the rapidly growing haloes in Cluster2 and Cluster3). If the actual cooling times then we would see no coloured points towards the right hand side of the plot. However, a number of coloured points (from Cluster2 and Cluster3) are seen to extend to the right hand side. This is because these haloes are not cooling as predicted and have longer than expected cooling times. The actual calculated values can be up to several Myr longer and given the halo growth rates this can lead to much more massive haloes developing before the actual cooling times are reached.

The increase in the cooling time of the gas means that the halo can continue to grow without collapsing. This has been shown in previous works, which in many cases looked at specific processes which increased cooling times, sometimes somewhat artificially, leading to the formation of (super-)massive stars through both the dissociation of the H_2 fraction (e.g. Latif et al. 2014b; Latif, Schleicher & Hartwig 2016; Regan, Johansson & Wise 2016; Regan et al. 2017), through the impact of baryonic streaming velocities (Tanaka & Li 2014; Latif, Niemeyer & Schleicher 2014; Hirano et al. 2017; Schauer et al. 2017) and through rapid assembly (Fernandez et al. 2014; Wise et al. 2019; Regan et al. 2020b).

3.4. Stellar Mass Predictions

We can further investigate the analytical impact of rapid assembly and to what extent it may impact on the initial mass function (IMF) of the stars that subsequently form by appealing to the fitting functions introduced in Hirano et al. (2014). Using their equation 14:

$$M_{\text{popIII}} = 100 M_{\odot} \left(\frac{\dot{M}_{\text{virial}}}{1.2 \times 10^{-3} M_{\odot} \text{ yr}^{-1}} \right) \quad (8)$$

we can calculate the expected stellar masses based on the mass inflow rates at the virial radius of our haloes. In Figure 6 we show the mass inflow rates as a function of halo radius. The virial radius for each halo varies with the mass of each halo. To guide the eye we have coloured the range of virial radii in grey - the median value for the virial radius of all haloes is approximately 100 pc and the average mass inflow rate within this region is $\dot{M} \sim 0.2 M_{\odot} \text{ yr}^{-1}$.

Now using the fitting function as given in Hirano et al. (2014) we find, given these high mass inflow rates, predicted stellar masses in excess of $10^4 M_{\odot}$ and

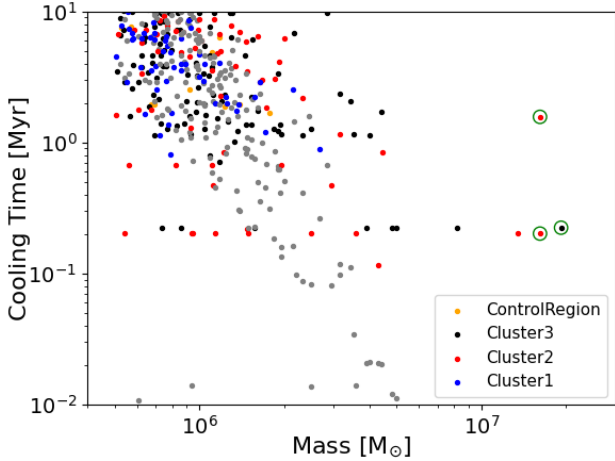


Figure 5. The cooling times from the analytic H_2 cooling function (Equation 4, grey dots) and from the numerically calculated values inside each halo (coloured dots). The analytically predicted H_2 cooling times for some halos, particularly those at higher masses, are significantly below those actually calculated numerically. Rather than cooling, the haloes are being dynamically heated due to rapid assembly. The star forming halos from Cluster2 and one from Cluster3 are circled. Cooling times in these haloes are additionally impacted by (radiative) feedback. In particular the cooling times for the star forming halo in the ControlRegion and the additional star forming halo from Cluster3 are impacted by feedback and are of order a hundred Myr and extend off the plot.

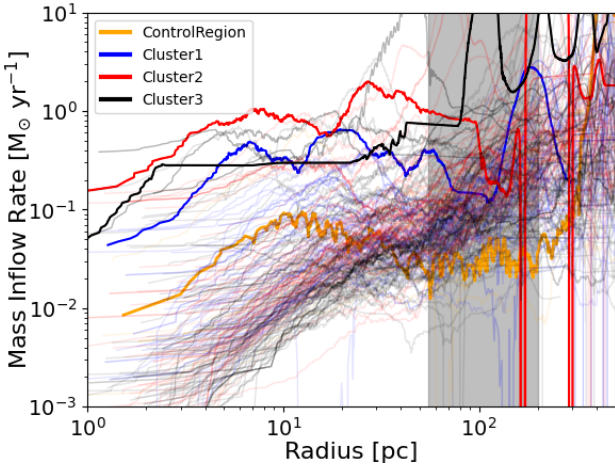


Figure 6. The mass inflow rates for each of the haloes identified as having cooling times shorter than one tenth of the Hubble time. The inflow rates cover a large range as expected given the diversity of environmental factors. The grey shaded region denotes the span in virial radii for the haloes plotted. Within this shaded regions the average mass inflow rate is approximately $0.2 M_\odot \text{ yr}^{-1}$.

possibly even exceeding $10^5 M_\odot$ for some haloes. In Figure 7 we show the predicted stellar masses for each halo as a function of halo mass. The fact that many haloes are growing at very high rates means that Eqn 8 predicts a large spread in final stellar masses. However, these results should be treated with caution and do not necessarily account for fragmentation in these haloes where bound clumps may fragment into smaller mass proto-stars or fluctuations in the mass inflow rate -

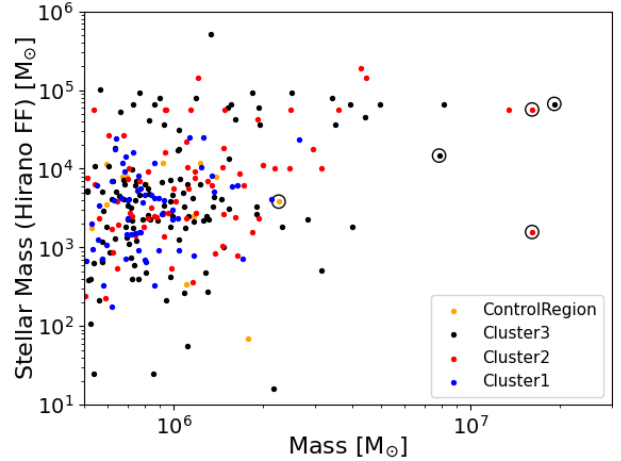


Figure 7. The fitting function from Hirano et al. (2014) ($M_{\text{popIII}} = 100 M_\odot \frac{\text{My}_{\text{virial}}}{1.2 \times 10^{-3} M_\odot \text{ yr}^{-1}}$) predict stellar masses in the range $M_* \sim 100 M_\odot$ up to $M_* \gtrsim 10^5 M_\odot$ consistent with what would be predicted for haloes with high accretion rates. These numbers should be viewed as upper limits as both fragmentation and limitations on stellar growth are difficult to quantify. Nonetheless, it appears we are tracing the tail of the PopIII IMF. The circled haloes again identify the five haloes currently undergoing star formation. Based on their mass infall rates (calculated at the virial radius) the fitting function predicts stellar masses between approximately $10^3 M_\odot$ and $10^5 M_\odot$. This is broadly consistent with, if somewhat higher than, what our detailed numerical simulations find in practice.

even though this fitting function was calibrated against mini-haloes in the same mass range (albeit ones not undergoing rapid assembly). The open circles in Figure 7 refer again to the haloes in which star formation has occurred. For these haloes the fitting function predicts stellar masses in range $10^3 M_\odot$ up to $10^5 M_\odot$. Within an order of magnitude these values are indeed correct and capture the top-heavy nature of the stellar masses formed. The actual stellar masses that are found in our simulations (see §4) are however somewhat lower. Nonetheless, the fitting function does point to a significantly more top-heavy IMF in these rare haloes forming in overdense peaks - consistent with recent results from Regan et al. (2020b) and Latif et al. (2022). Note also that the orange points (ControlRegion) are at least an order of magnitude below the points from Cluster2 and Cluster3.

3.5. Radial Profiles of the Star Forming Haloes

In Figure 8 we plot the radial profiles of the first halo to undergo gravitational collapse in each of the ControlRegion, Cluster1, Cluster2 and Cluster3. In the panels, starting in the bottom left and moving clockwise, we plot the temperature, number density, H_2 fraction and the mass inflow into the halo centre. The profiles of each cluster are broadly similar. The temperature at the centre of each halo is between 600 K and 800 K typical of galaxies hosting the formation of metal-free stars with virial temperatures of close to 2000 K. The density profile of each halo is roughly isothermal with some flattening of the profile towards the halo centre as the gas becomes pressure supported. H_2 fractions saturate at

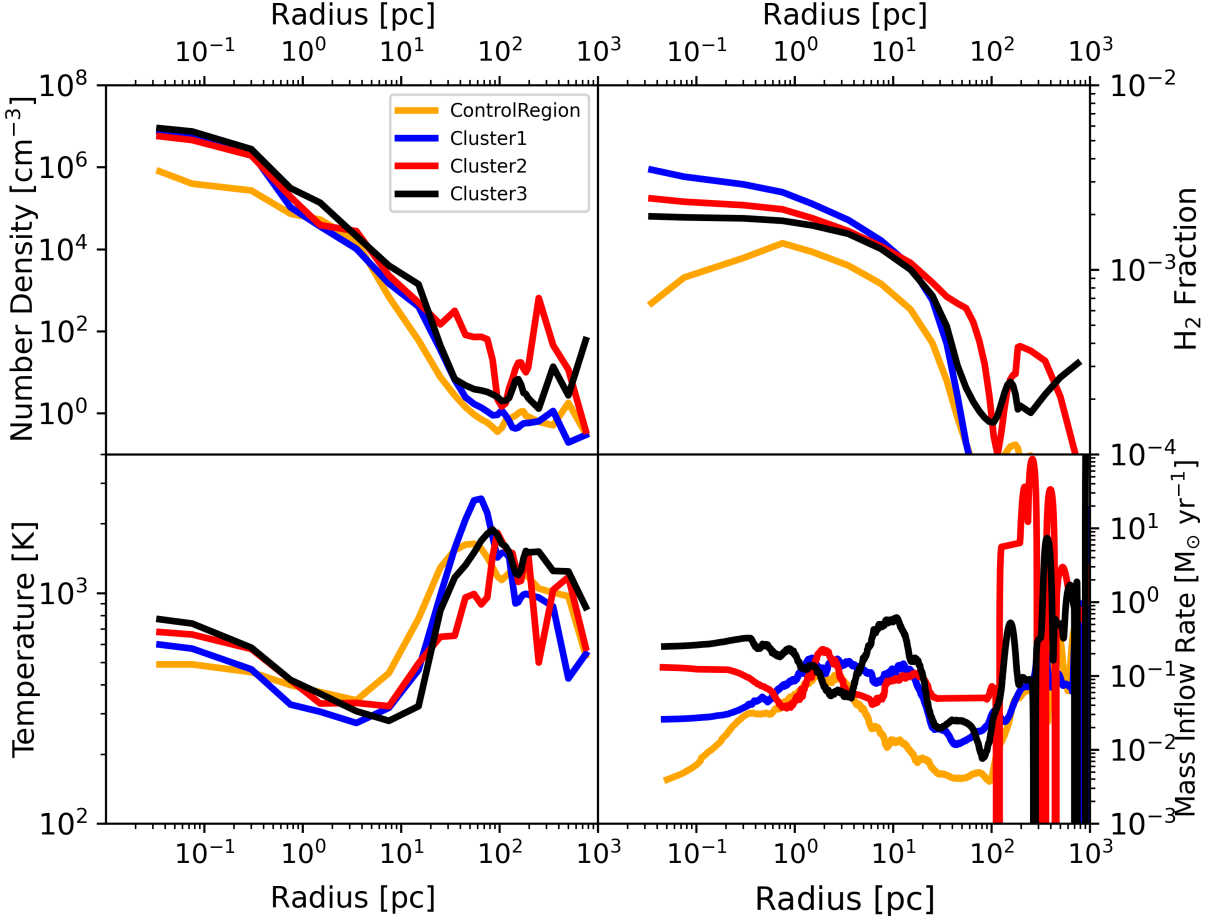


Figure 8. Radial profiles for the four haloes identified as undergoing first gravitational collapse - one from each of the ControlRegion, Cluster1, Cluster2 and Cluster3. Starting in the lower left panel and moving clockwise we show the gas temperature, gas number density, H_2 fractions and the mass accretion rates into the halo centre. The virial temperature of each halo is approximately 2000 K well below the threshold for Lyman- α cooling meaning that cooling is dominated by H_2 emission line cooling. Temperatures in the centre of each halo are approximately 700 K. Gas number densities follow an approximately isothermal profile with H_2 fractions consistent with their equilibrium value of 10^{-3} . The accretion rates into the halo centres are remarkably high with values close to, or in excess of, $0.1 M_{\odot} \text{ yr}^{-1}$ down to small radii. Such high accretion rates in the halo centre indicate that stars with “super-massive” characteristics may initially form (e.g. Woods et al. 2019). The virial radius for the four regions are; ControlRegion : 45 pc, Cluster1 : 55pc, Cluster2 : 105pc, Cluster3 : 105pc.

approximately 2×10^{-3} . The mass inflow rates into the centre of each halo are remarkably high however and are much higher than expected for a typical PopIII forming halo (Hirano et al. 2014). The mass inflow rates into the centre of each halo are in the realm of that expected for supermassive star formation (Haemmerlé et al. 2018b). Although, as we will see and as was found in Regan et al. (2020b), such high mass inflow rates are difficult to sustain (as stellar accretion rates) for the entire (pre-main sequence) evolution of the star.

A recent study by Latif et al. (2022) (L22) found a rare halo collapsing at the nexus of a number of converging cold flows at high redshift ($z \sim 26$). For their halo they found that the pressure support from turbulent velocities significantly exceeded the gravitational compression. This allowed the halo to delay collapse until the halo had a mass of $M_{\text{halo}} = 4 \times 10^7 M_{\odot}$. This is similar, albeit a factor of a few, more massive than our most massive halo. In their study they found turbulent velocities of order a few tens of km s^{-1} .

In Figure 9 we show the radial velocity (solid lines), turbulent velocities (dashed lines), sound speed (dotted lines) and rotational velocities (dashdot with ‘x’ marker)

at the same epoch as in Figure 8. The rotational velocities are calculated by taking the moments of the inertia tensor of the gas at varying radii from the centre (e.g. Regan & Haehnelt 2009) with the turbulent velocities calculated by subtracting both the bulk and radial velocities away from the raw cell velocities. This likely gives an upper limit to the level of turbulent velocities in the halo. In all cases the rotational velocities dominate, indicating gas that is strongly rotationally supported. Similarly to L22 we see evidence of supersonic radial inflows but our turbulent velocities are approximately a factor of between three and five times lower than the turbulent velocities found in L22. However, the haloes we show here are merely the first to collapse and hence not representative of the rarer haloes which may be required for turbulent velocity support to take hold. Across the mass spectrum of all haloes sampled we see strong evidence for rapid assembly being the primary driver for delaying gravitational collapse and allowing for the build-up of more massive haloes (and hence larger accretion rates onto the halo centres). It is likely, and indeed L22 reach this broad conclusion, that their halo is a rarer manifestation of the rapid assembly process with rapid global

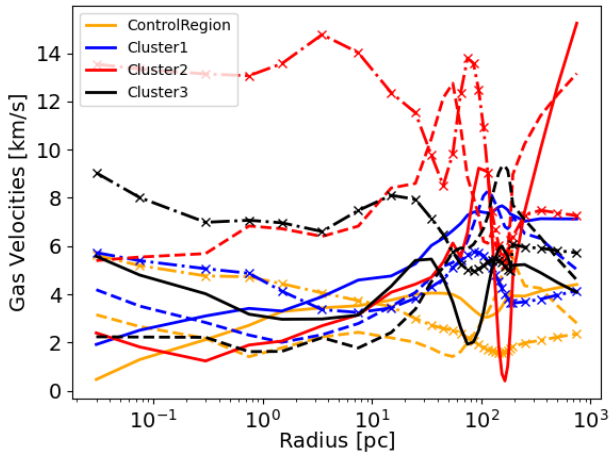


Figure 9. Gas velocities from the first halo to collapse in the ControlRegion (orange), Cluster1 (blue), Cluster2 (red) and Cluster3 (black). Solid lines mark radial inflow velocities, dashed lines the turbulent velocities and dashdot with ‘x’ markers the rotational velocities. The flow is almost always supersonic with radial inflow velocities exceeding the sound speed at almost all radii. In all cases the gas is rotationally supported with the rotational velocities dominating over all other velocity components. Turbulent velocities (dashed lines) are sub-dominant in all cases.

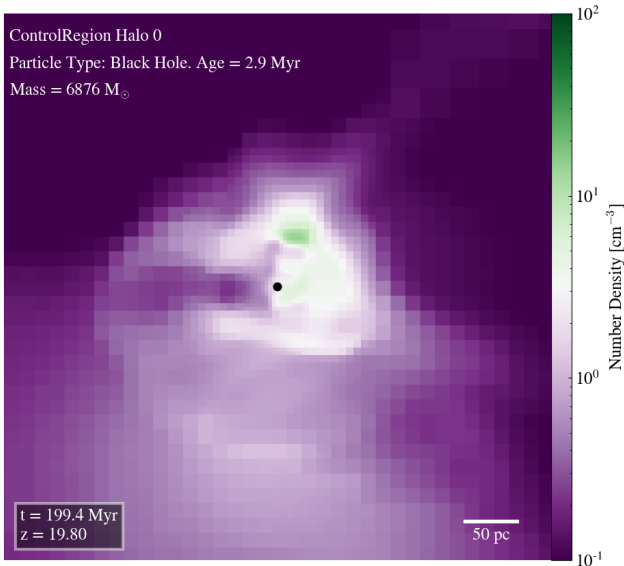


Figure 10. The first halo to collapse and form a star in the ControlRegion forms a SMS initially due to the initial large mass inflow onto the stellar surface. This large mass inflow quickly grows the star to approximately $6000 M_{\odot}$. The star’s short lifetime (500 kyr) means that it quickly collapses into a black hole. The black hole sits at the centre of the halo but is currently quiescent surrounded by relatively low density gas.

inflows driving the formation of massive stars in (rare) massive haloes.

In summary, for the first haloes to collapse in our sample we observe rotationally supported gas dominating which is also likely to impact the mass of the stars formed unless the rotational support can be transported away efficiently.

4. THE ONSET OF STAR FORMATION

Having found that Cluster2 and Cluster3 show a preponderance of rapidly accreting haloes we proceed to evolve Cluster 2 and Cluster3 beyond the initial phase of gravitational collapse. This is also necessary as we need to focus our computational resources. We additionally continue to evolve the ControlRegion as a comparison against a ‘normal’ region. Cluster 2 is the first halo to collapse and undergo star formation at $z = 23.06$ followed by Cluster3 at $z = 22.31$. The ControlRegion meanwhile forms its first star at $z = 20.00$. In Figure 10, Figure 11 and Figure 12 we show visualisations of each of the star forming haloes. The visualisation for the ControlRegion is created at $z = 19.80$ at which point the massive PopIII star has collapsed into a MBH. It’s current age is 2.9 Myr. The star forming haloes in Cluster2, of which there are two, are separated by 33 kpc (physical). The visualisations (centred on the stars in each case) are both created at $z = 22.8$ which is more than 2 Myr after the formation of the first star. As can be seen from the visualisations both stars are embedded within an overdensity. The results for the star forming haloes in Cluster3 are broadly similar (see Figure 12) with again two different star forming haloes emerging. In this case however the separation between the haloes is significantly less with a separation of less than 1 kpc. While the separation both in time and space between the haloes is (marginally) consistent with the synchronised pair scenario the haloes are both too small and there is no background LW radiation field to support the mechanism (Dijkstra et al. 2008; Visbal, Haiman & Bryan 2014b; Regan et al. 2017).

In Figure 13, Figure 14 and Figure 15 we show the accretion rates and mass growth history of each of the five stars to form as well as their transitions into massive PopIII and black holes where appropriate. In Figure 13 (ControlRegion) we can see that the initial (merger triggered) star formation results in a SMS with growth rates exceeding the critical value. After approximately 50 kyr the growth rate of the star drops off as the gas is accreted by the star. At this point the star has grown to a mass of $6876 M_{\odot}$. In Figure 14 we show the accretion rates and masses of the two stars from Cluster2. Both stars initially accrete extremely rapidly with mass accretion rates well in excess of $10^{-3} M_{\odot} \text{ yr}^{-1}$ which we use here as the critical rate for SMS formation (Haemmerlé et al. 2018b). However, in both cases this rapid accretion is short-lived and ceases a few tens of kiloyears after formation. At this point both stars contract towards the main sequence and become massive PopIII stars - similar to the evolution seen in the ControlRegion halo. The large masses of these objects also means that their lifetimes are extremely short. We calculate the lifetimes of these massive PopIII stars by fitting to the functional form given by Schaerer (2002). Given their masses these massive PopIII stars directly collapse into massive black holes after a few hundred kiloyears. Similar to the case of when the stars were SMSs the accretion rates remain extremely low following their transition into MBHs. One of the MBHs (the MBH with a mass of $5101 M_{\odot}$) does accrete intermittently with rates up to $10^{-3} M_{\odot} \text{ yr}^{-1}$ but these rates hardly effect the mass. The accretion does give rise to small amounts of feedback however which we discuss in the next section.

The first star to form in Cluster3 forms as a PopIII star

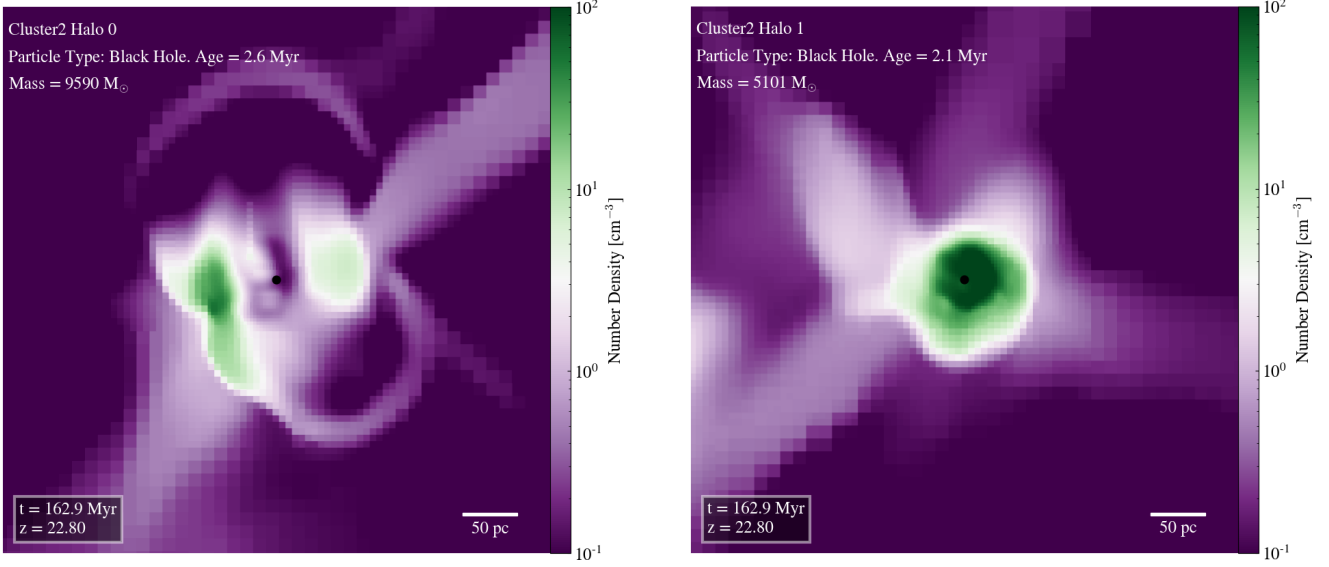


Figure 11. Two stars form in two separate haloes in Cluster 2 within the 2.6 Myr following the formation of the first star (left panel). Both stars accrete extremely rapidly and using the fitting formula from [Schaerer \(2002\)](#) the lifetimes of these massive PopIII stars are 300,000 and 600,000 years respectively. Following their stellar lifetimes both stars directly collapse into massive black holes with masses of $9590 M_{\odot}$ and $5101 M_{\odot}$ respectively.

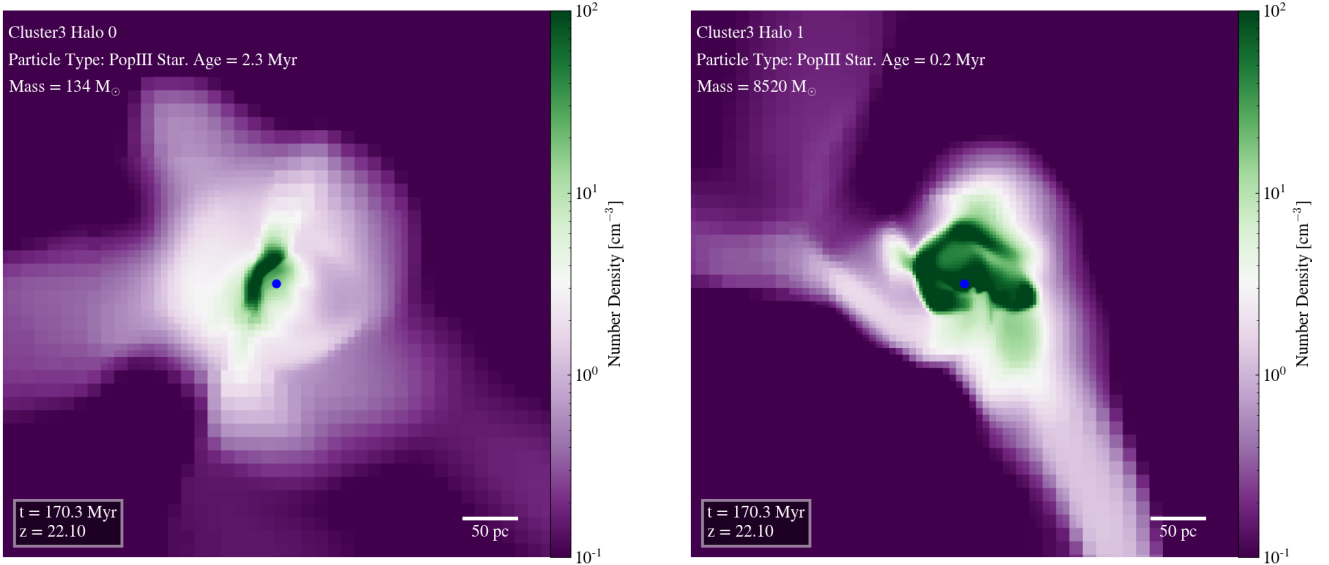


Figure 12. Similar to Cluster 2 with two stars in two separate haloes within the Cluster 3 environment. The first star to form in this case was a PopIII star with an (IMF sampled) mass of $134 M_{\odot}$. In our simulations PopIII stars do not accrete as their spatial scale is below our resolution scale. The lifetime of a star of this mass is calculated to be 2.6 Myr and has therefore not yet collapsed into a black hole. The other star is also a massive PopIII star with a current age of 0.2 Myr. It's calculated lifetime is 0.6 Myr (due to it's extreme mass) and it will collapse into a massive black hole at that time.

with an IMF sampled mass of $134 M_{\odot}$ - it's initial accretion rate is below that required for SMS formation and so a PopIII star is formed from the start. PopIII stars do not accrete in our simulations and hence this star remains a PopIII star with an unchanging mass. The calculated age of the star is 2.6 Myr and at this stage (current age = 2.3 Myr) the star is still in that phase. The other star to form (in a separate halo) has an initial accretion rate exceeding the critical threshold rate and therefore forms a SMS (see [Figure 12](#)). In a similar vein to the stars in the ControlRegion and Cluster2 the initial accretion rate is not maintained and once the gas in the imme-

diately vicinity of the SMS is accreted the accretion rate plummets and the star contracts to the main sequence. The SMS, which is the second star to form in Cluster3, has a mass of $8676 M_{\odot}$ when it transitions to a massive PopIII star as shown in [Figure 15](#). This star's lifetime is calculated at 0.6 Myr (current age = 0.2 Myr) and will directly collapse into a black hole at that point. We will report the finding of the growth and dynamics of these first MBHs in a subsequent paper.

4.1. Merger Triggered Star Formation at High- z

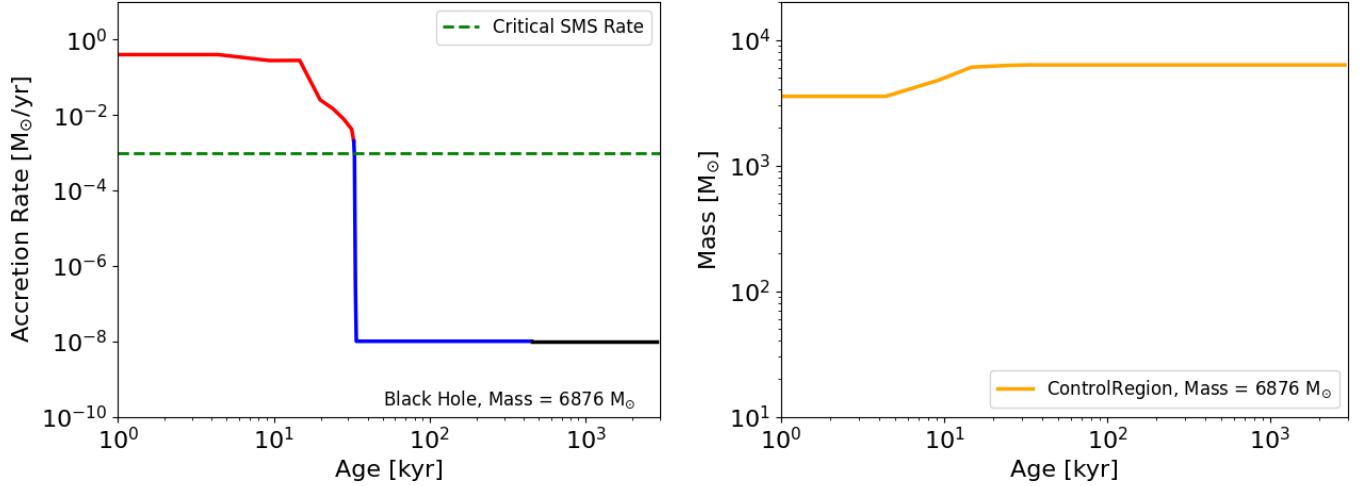


Figure 13. In the left hand panel we show the accretion rate onto the first star to form in the ControlRegion. The star initially and rapidly accretes matter onto the stellar surface at rates significantly exceeding the critical rate. This causes the star to move to the red, puff up, and become a SMS. However, the high accretion rates are not maintained and after approximately 50,000 years the star transitions to the blue and become a massive PopIII star. The star subsequently collapses into a massive black hole. Right Panel: The mass history of the star/MBH. The rapid increase in mass at early times is the dominant driver in determining the final mass of the star.

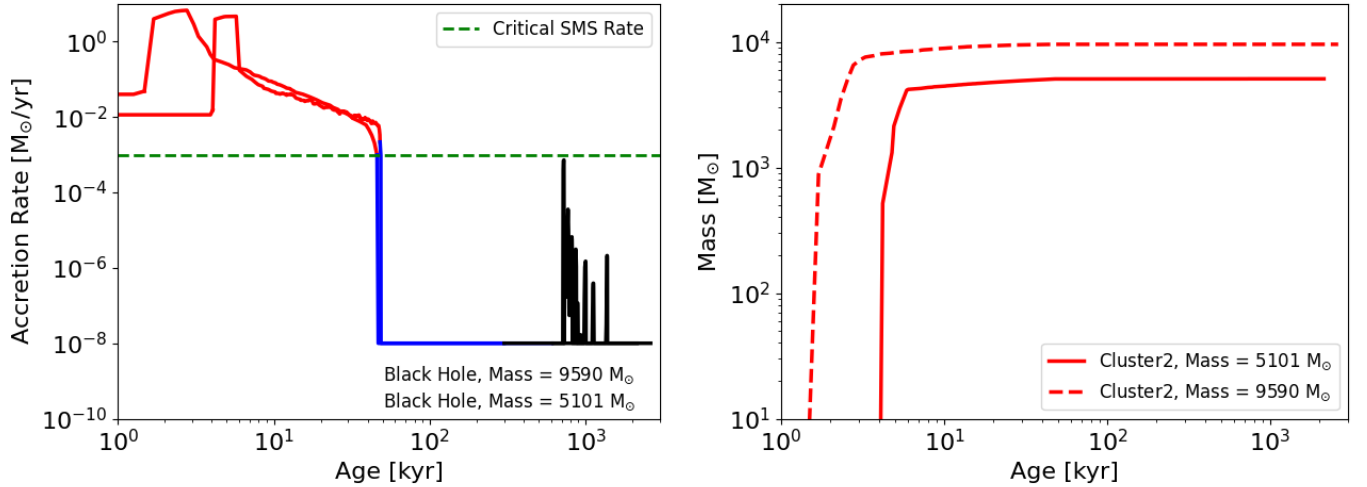


Figure 14. In the left hand panel we show the accretion rates for the two objects that have formed in Cluster2. The evolution of both stars follows a similar trajectory to the star that forms in the ControlRegion. Both stars collapse into MBHs at the end of the stellar lifetime. One of the black holes exhibits intermittent accretion approximately 1 Myr after formation as it passes through some dense material (see right hand panel of Figure 11). However, the accretion is relatively short lived and has little or no impact on the mass of the black hole. Right Panel: The mass history of both objects. Again the rapid increase in mass at early times is the dominant driver in determining the final mass of the star. The small accretion activity seen at approximately 1 Myr in the left panel has no appreciable effect on the mass of the black hole.

The overdense nature of Cluster2 and Cluster3 combined with the relatively youthful age of the Universe at this epoch means that mergers are common (the Universe at $z \sim 20$ is approximately 10,000 times more dense than today's Universe). Examining again Figure 2 we can see that the star forming halo in the ControlRegion, one of the star forming haloes in Cluster2 and one of the star forming haloes in Cluster3 show step increases in mass either just after star formation or just prior to star formation (the point of star formation is marked by the star symbol). In each of these cases a major merger takes place resulting in the rapid flow of gas to the halo centre. The mass inflow rates due to these mergers vary between $10^{-3} M_{\odot} \text{ yr}^{-1}$ and $1 M_{\odot} \text{ yr}^{-1}$ (see Figure 6 and Figure 8). The rapid inflow of gas as a result of the merger is

however time limited and in each case, across all three of these haloes, lasts for approximately 50 kyr. The combination of this timescale and the inflow rates leads to final stellar masses of a few thousand solar masses for two of the three haloes. The third halo (Cluster3) which shows a steep growth profile actually forms a star prior to the merger (see below).

Following the merger and the subsequent star formation we see the inflow rates subside (see lower right panel of Figure 16) and fall to values as low as $\sim 10^{-8} M_{\odot} \text{ yr}^{-1}$. For the other two star forming haloes shown in Figure 2, which show more modest growth, albeit to higher halo masses, as opposed to the steep ascent, the resulting stellar masses are actually quite similar (these two haloes form stars with masses of $5101 M_{\odot}$ and 8520

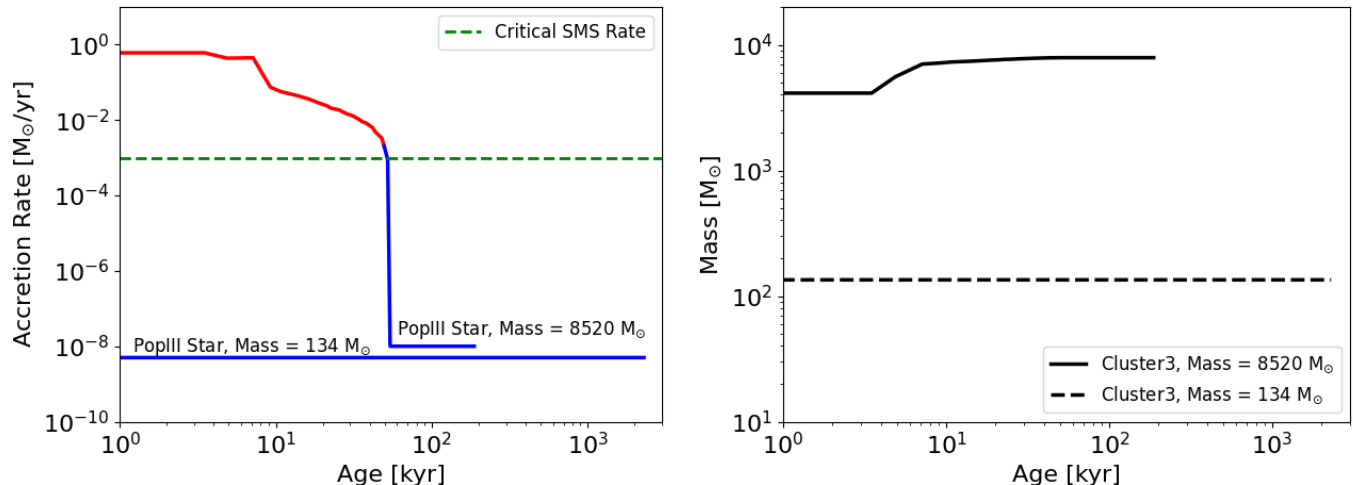


Figure 15. In a very similar pattern to Cluster2, in the left hand panel we show the accretion rates for the two objects that have formed in Cluster3. In the case of Cluster3 however the first star forms as a PopIII star (with a mass of $134 M_{\odot}$) while the second star forms as a SMS. The SMS subsequently contacts to the main sequence and evolves into a massive PopIII star with a mass of $8520 M_{\odot}$. Both stars are currently still in their stellar phases. Right Panel: The mass history of both stars - the first star to form (a PopIII star) does not accrete and has the same mass throughout. The second star (initially a SMS) grows rapidly in mass before contracting to the main sequence.

M_{\odot} respectively). These two, more modestly growing, haloes are positioned at the nexus of multiple filaments (see Figure 17) and grow to close to the atomic cooling threshold before star formation commences. We may be witnessing a bi-modality emerging.

Rapid growth drives very massive star formation in all cases. If a major merger occurs (which accelerates the process) then a massive star forms from the rapid inflow due to the merger. In the absence of a major merger but in the presence of multiple minor mergers rapid assembly dominates, preventing normal PopIII star formation, resulting nonetheless in a massive star.

In any case for, at least some of, the first haloes to form, star formation is driven by *merger triggered star formation*. A major merger of mini-haloes results in inflow rates sufficient to drive the formation of a SMS but not sufficient to stop the star from returning to the main sequence after a few tens of kiloyears. The halo with the $134 M_{\odot}$ PopIII star is more standard among the five star forming haloes (bottom left panel of Figure 17). Looking again at Figure 2 we can clearly see that this halo also suffers a major merger at $z \sim 22.2$. However, in contrast to at least three of the other halos this halo forms along a filament as opposed to at the junction of several filaments. While this halo clearly experiences a merger, star formation occurs prior to the merger and as a result the mass inflow rates do not exist to drive SMS formation in the first instance. Instead in this case a PopIII star forms with a (stochastically calculated) mass of $134 M_{\odot}$.

In summary, merger triggered star formation drives SMS star formation in two out of our five haloes, in a further two haloes rapid assembly grows the host halo to close to the atomic cooling threshold before star formation occurs. In the final halo a more normal PopIII star forms just prior to a major merger. There are strong parallels with our merger triggered star formation and the proposed process for SMBH formation outlined by Mayer et al. (2010). Mayer et al. (2010) proposed a scenario where a major merger between two massive galaxies (at $z \sim 10$) results in the direct formation of a SMBH. In

our case we observe a similar process, acting on smaller mass scales, resulting in the formation of a SMS.

4.2. Profiling the Stellar Environment

In Figure 16 we show the radial profiles for the temperature, electron fraction, number density and mass inflow rates within the host halo of each star forming halo in each cluster (orange for the ControlRegion, red for Cluster2 and black for Cluster3). Of the five stars which have formed in the simulations three have since collapsed into MBHs with one residing in the ControlRegion with a mass of $6876 M_{\odot}$ and two others in Cluster 2 with masses of $9590 M_{\odot}$ and $5101 M_{\odot}$ respectively. All three MBHs are currently quiescent although the lighter MBH in Cluster2 has experienced some modest accretion over last few hundred kiloyears. This may not be surprising since the gas surrounding the lighter MBH in Cluster2 is relatively cold and much denser compared to the gas surrounding the more massive MBH. The gas is in both cases strongly ionised with electron fractions close to 0.1. This is likely due to the recent stellar feedback which would have ionised the gas in the immediate vicinity of the stars (prior to the black hole phase at which point feedback ceased as accretion is essentially nonexistent).

The most strongly ionised gas is that surrounding the stars in Cluster3 which are both still in their stellar phase. For both of these stars the gas is highly ionised (at least in the immediate vicinity of the star) due to the radiative feedback from the PopIII star with a mass of $134 M_{\odot}$ and the thermal feedback from the massive PopIII star with a mass of $8520 M_{\odot}$. We implement thermal feedback for all massive PopIII stars with masses in excess of $500 M_{\odot}$. As noted in §2.6 we do this as the computational cost of radiative feedback for such massive stars makes tracking that radiation spectrum computationally intractable and instead we turn to thermal feedback. We do not expect this to adversely effect our results in general since radiation even from such massive stars is not expected to propagate beyond the immediate vicinity of these stars (Woods et al. 2021; Jaura et al.

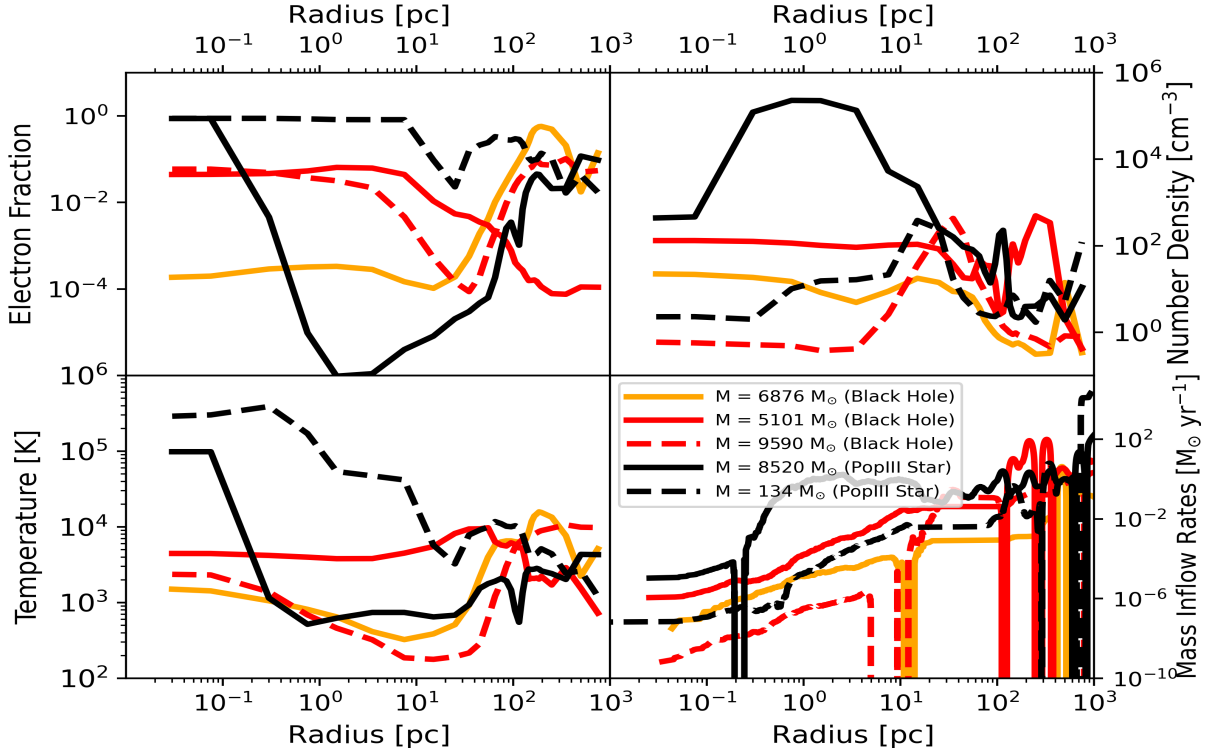


Figure 16. Radial profiles for the host halo in each cluster which hosts a star or MBH. Orange lines for the ControlRegion, red lines for Cluster2 and black lines for Cluster3. The gas surrounding the MBHs is cooler due to the lack of radiative feedback from the non-accreting MBHs. Electron fractions are very high within 0.1 pc of each object but drop off for the cases of all objects apart from the PopIII star with a mass of $134 M_{\odot}$. Number densities in the host haloes are relatively low with the exception of the halo hosting the $8520 M_{\odot}$ PopIII star. This star is surrounded, at a distance of less than 1 pc, by high density gas which, depending on subsequent angular momentum, may be accreted on the MBH that will form with a few hundred kiloyears. Mass inflow rates into this host halo are also favourable exceeding $10^{-2} M_{\odot} \text{ yr}^{-1}$ within 1 pc of the halo centre.

2022). The ionised fraction for the lighter PopIII star does extend beyond the vicinity of the star in this halo due to the relative underdensity of gas in the halo and the relatively low mass of the halo.

Infact the density of gas surrounding most of the stars and MBHs is comparatively low (less than 10^2 cm^{-3} for four of the five objects). Only for the (non-accreting) $8520 M_{\odot}$ star does the number density exceed 10^2 cm^{-3} . This will mean that the black hole that forms at the end of this star’s stellar life (in approximately 0.4 Myr) will have the potential to accrete a substantial mass of gas. This supposition is further supported by examining the lower right panel of Figure 16. In that panel we can see that the mass inflow rates for this halo are the highest of all four haloes with gas inflow rates of at least $\dot{M} \sim 10^{-3} M_{\odot} \text{ yr}^{-1}$ extending all the way to the centre of the halo. Each of the other haloes now show relatively weak mass inflow rates which supports the lacklustre accretion rates seen for the two black holes in Cluster2.

4.3. Numerical Caveats

As with any numerical simulation attempting to model complex processes such as star formation there are inevitable caveats. The primary caveat in these simulations is resolution. Our maximum resolution here is set by the size of our smallest grid cell which is approximately 0.05 pc (physical). This is significantly above the scale at which star formation takes place and at densities many orders of magnitude below the actual formation threshold. For example Prole et al. (2022) see no numerical

convergence in their PopIII star formation simulations even at densities up to $n \sim 10^{20} \text{ cm}^{-3}$. The results of Prole et al. (2022) suggest that our results here may be missing significant fragmentation of the central core and that many PopIII stars may form in these first mini-haloes in contrast to the one SMS we see in our haloes.

However, this must be weighed against the fact that these haloes here experience mass inflow rates many orders of magnitude higher than average and the fact that our sink particle calculated masses are below those predicted by the fitting functions of Hirano et al. (2014) for example. What is not in doubt is that we are modelling rare haloes, undergoing rapid assembly with large mass inflows, and that they likely produce very massive stars or dense stellar clusters containing an equivalent mass in stars (Prole et al. 2022). Further zoom-in simulations at significantly enhanced spatial and mass resolution will be required in the future to probe the different outcomes in greater detail.

5. DISCUSSION AND CONCLUSIONS

Here we introduce the BlackDemon simulations. The rationale driving these simulations is to investigate the formation of MBH seeds in overdense regions of the embryonic universe in a self-consistent manner. Three distinct clusters (each $1 \text{ h}^{-1} \text{ Mpc}$ comoving on the side) are identified and resolved with particle masses of $M_{\text{part}} \sim 2.3 \times 10^3 M_{\odot}$ and maximum spatial resolutions of $\Delta x \sim 0.05 \text{ pc}$ (physical at $z = 20$). We additionally evolve a ControlRegion within a mean density region of

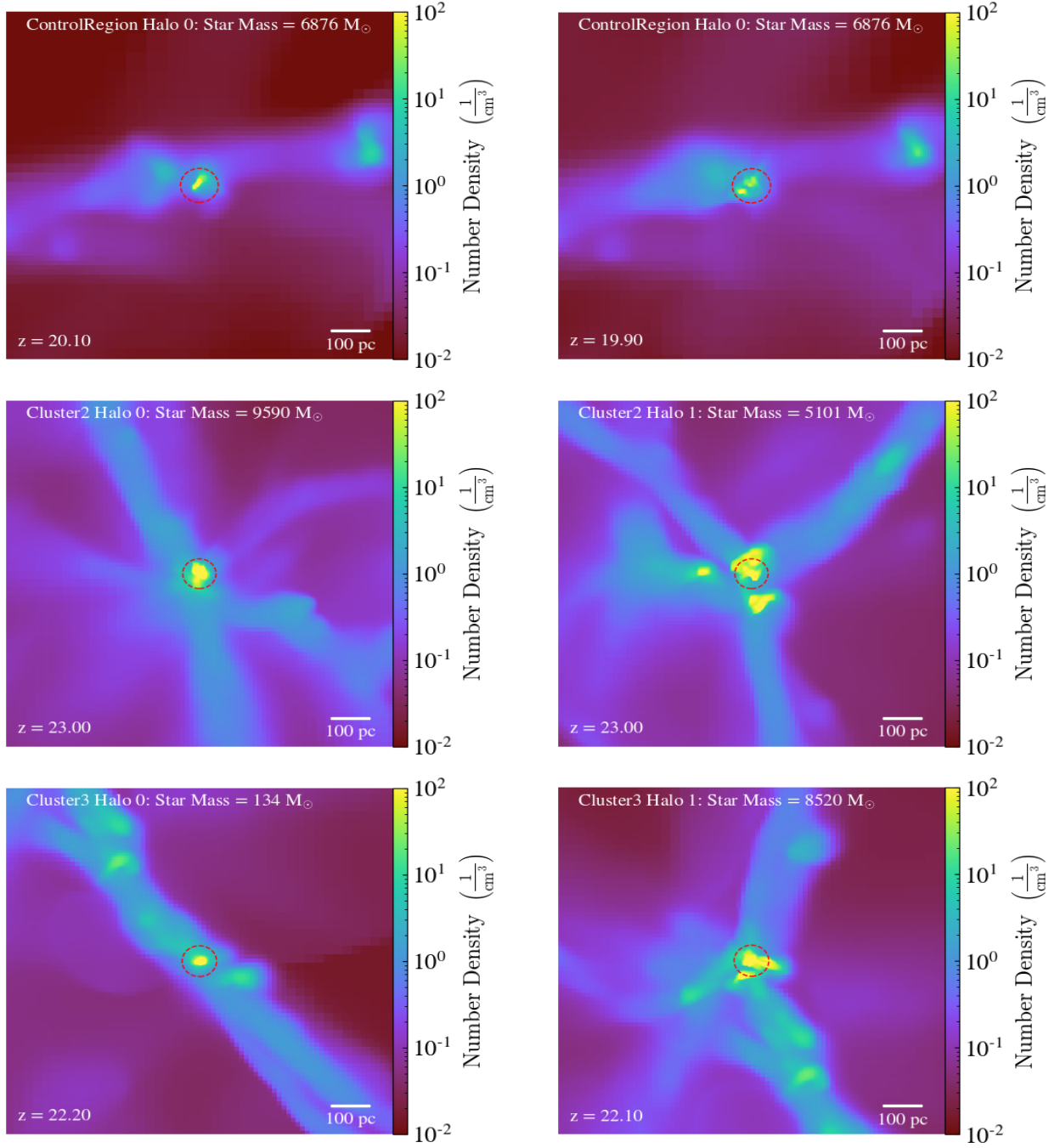


Figure 17. The large scale environment surrounding each of the star forming haloes at the output redshift closest to the onset of star formation. The red dashed circle in each case marks the star forming halo. *Top row:* The first row shows the conditions operating around the ControlRegion halo. There is only one star forming halo in the ControlRegion and so we show two outputs. Between $z \sim 20.10$ and $z \sim 19.90$ a merger occurs between the most massive (circled) halo and a smaller halo to its immediate left. The merger actually causes the original halo to be disrupted but in doing so also triggers star formation (at $z \sim 20$). *Middle row:* The second row shows the conditions around the two star forming haloes in Cluster2. Each halo is positioned at the nexus of intersecting filaments. Halo 0 (middle left panel) forms a star due to triggered star formation while Halo 1 (middle right panel) experiences more modest growth and forms a star prior to the halo reaching the atomic cooling limit. *Bottom row:* The third row shows the conditions around the two star forming haloes in Cluster3. In Halo 0 (bottom left panel), which is located, mid-way along a filament a $134 M_{\odot}$ star forms. In Halo 1 (bottom right panel) the star forming halo is located again at the nexus of a number of filaments which delays star formation until the halo approaches the atomic cooling limit.

the parent box for comparison. We find that of the three (overdense) clusters modelled, Cluster2 and Cluster3 have a significant fraction of haloes growing at rates that exceed the critical growth rate and show the largest deviations from a predicted Press-Schechter halo mass function.

As a result the cooling times of the gas for a significant number of haloes in Cluster2 and Cluster3 are longer than the analytically predicted values, these longer cooling times allow larger Jeans masses to develop lending support to the premise that these haloes will produce more massive stars. We find that the first halo to collapse (at $z = 23.06$) has a mass of $1.04 \times 10^7 M_{\odot}$ when it first undergoes gravitational instability. This mass is just short of the atomic cooling threshold at this redshift ($M_{\text{atm}} \sim 1.5 \times 10^7 M_{\odot}$ at $z \sim 23$).

We continue the evolution of the ControlRegion, Cluster2 and Cluster3 beyond the formation of the first star in each case and report the results approximately 2 Myr after first star formation in each region. After 2 Myr two MBHs reside in two separate haloes in Cluster2 with masses of $9590 M_{\odot}$ and $5101 M_{\odot}$ respectively. In both cases initially a SMS formed but in both cases the SMS contracted to the main sequence as critical accretion was not maintained. Both MBHs are currently quiescent. Cluster3 shows a broadly similar result. In Cluster3, two PopIII stars reside with masses of $134 M_{\odot}$ and $8520 M_{\odot}$ respectively. Both objects are currently still in their stellar phases and have not yet collapsed to form MBHs. Interestingly the ControlRegion also forms a SMS in the first halo to collapse in that region. As discussed in §4.3 higher resolution simulations of these environments will ideally be required to resolve the formation of a molecular core (e.g. Prole et al. 2022) and to probe fragmentation below our current resolution limit.

In investigating the driver of the massive star formation in each halo we found that major merger triggered star formation occurred in two haloes (one in the ControlRegion and one in Cluster2). In another two cases (one in Cluster2 and one in Cluster3) massive star formation occurred following rapid assembly up to just short of the atomic cooling limit in haloes at the junction of multiple filaments. In the fifth and final case a ‘normal’ PopII star formed.

What then can we extract from the initial results of these simulations? The first result is that haloes evolving inside an overdense region, in the case of Cluster2 and Cluster3 a 4-sigma fluctuation, experience large mass infall rates driven by the numerous minor mergers they experience. Secondly, the minor mergers in many cases result in dynamical heating mitigating against early PopIII star formation allowing the build up of larger halo masses. Thirdly, major mergers once the masses of the haloes approach a few times $10^6 M_{\odot}$ can also drive SMS star formation. The mergers at this point push the gas past the point of gravitational instability and result in massive star formation. The large gas inflows from the merger are of the order of $0.01 - 1 M_{\odot} \text{ yr}^{-1}$ in the newly formed halo centre and trigger SMS formation. These rapid mass inflows are however not sustained and after approximately 50 kyr the mass inflow rates subside and the SMS contacts back to the main sequence forming a massive PopIII star with a mass in the range $5,000 - 10,000 M_{\odot}$. Given the over-

dense environment further major mergers may however be expected which will replenish the gas reservoir at the centre of these haloes. At the time of reporting three of the first stars to form have transitioned into MBHs with masses of $5101 M_{\odot}$, $6876 M_{\odot}$ & $9590 M_{\odot}$. The MBHs are currently quiescent (though one showed short-lived accretion) and must await further gas inflows before being able to grow further. The two other stars remain in their PopIII stellar phase with masses of $134 M_{\odot}$ and $8520 M_{\odot}$ respectively.

What we are probing here is the high end tail of the PopIII mass spectrum. These are stars forming in rare, over-dense, environments experiencing mass infall rates 10 's to 100 's of times the average values. The star formation is being driven by the mergers of building block sub-embryonic galaxies - a regime previously almost universally unexplored. The first generation of results from Bromm, Coppi & Larson (2002) and Abel, Bryan & Norman (2002) predicted that the first stars would be very massive with masses close to $1000 M_{\odot}$. Subsequent and more detailed calculations at higher resolution and updated chemistry solvers showed that fragmentation of the initial gas cloud reduced the final masses considerably (e.g. Clark, Glover & Klessen 2008; Turk, Abel & O’Shea 2009). However, it now appears that by probing the high-end tail of the distribution that the very first stars may indeed have been exceptionally massive with final masses well in excess of $10^3 M_{\odot}$.

ACKNOWLEDGMENTS

JR acknowledges support from the Royal Society and Science Foundation Ireland under grant number URF\R1\191132. JR also acknowledges support from the Irish Research Council Laureate programme under grant number IRCLA/2022/1165. JR acknowledges that the results of this research have been achieved using both EuroHPC JU (Karolina) and DECI resources (Barbora) supported by the IT4Innovations National Supercomputing Center based in the Czech Republic. JR also wishes to acknowledge the DJEI/DES/SFI/HEA Irish Centre for High-End Computing (ICHEC) for the provision of computational facilities and support on which a portion of these simulations were run. Additionally portions of the simulations were run on the Frontera Supercomputer based at the Texas Advanced Computing Center, US. The freely available plotting library MATPLOTLIB (Hunter 2007) was used to construct numerous plots within this paper. Computations and analysis described in this work were performed using the publicly-available Enzo (Bryan et al. 2014; Brummel-Smith et al. 2019) and yt (Turk et al. 2011) codes, which are the product of a collaborative effort of many independent scientists from numerous institutions around the world. Their commitment to open science has helped make this work possible. JR finally thanks John Wise for constructive discussions and feedback on this manuscript and in general over many years! We thank the anonymous referee for a constructive report.

REFERENCES

- Abbott B. P. et al., 2016, Physical Review Letters, 116, 061102
 Abel T., Anninos P., Zhang Y., Norman M. L., 1997, New Astronomy, 2, 181

- Abel T., Bryan G. L., Norman M. L., 2000, *ApJ*, 540, 39
- Abel T., Bryan G. L., Norman M. L., 2002, *Science*, 295, 93
- Agarwal B., Regan J., Klessen R. S., Downes T. P., Zackrisson E., 2017, *ArXiv e-prints*
- Alexander T., Natarajan P., 2014, *Science*, 345, 1330
- Alvarez M. A., Wise J. H., Abel T., 2009, *ApJ*, 701, L133
- Anninos P., Zhang Y., Abel T., Norman M. L., 1997, *New Astronomy*, 2, 209
- Baldassare V. F., Dickey C., Geha M., Reines A. E., 2020, *arXiv e-prints*, arXiv:2006.15150
- Barkana R., Loeb A., 2001, *Phys. Rep.*, 349, 125
- Beckmann R. S. et al., 2022, *arXiv e-prints*, arXiv:2211.13301
- Behroozi P. S., Wechsler R. H., Wu H.-Y., 2013, *ApJ*, 762, 109
- Bellovary J. M., Governato F., Quinn T. R., Wadsley J., Shen S., Volonteri M., 2010, *ApJ*, 721, L148
- Bromm V., Coppi P. S., Larson R. B., 2002, *ApJ*, 564, 23
- Brummel-Smith C. et al., 2019, *The Journal of Open Source Software*, 4, 1636
- Bryan G. L., Norman M. L., 1998, *ApJ*, 495, 80
- Bryan G. L., Norman M. L., O'Shea B. W., Abel T., Wise J. H., Turk M. J., The Enzo Collaboration, 2014, *ApJS*, 211, 19
- Chabrier G., 2003, *PASP*, 115, 763
- Chen P., Wise J. H., Norman M. L., Xu H., O'Shea B. W., 2014, *ApJ*, 795, 144
- Chiaki G., Chon S., Omukai K., Trinca A., Schneider R., Valiante R., 2023, *arXiv e-prints*, arXiv:2303.01762
- Chiou Y. S., Naoz S., Marinacci F., Vogelsberger M., 2018, *MNRAS*, 481, 3108
- Clark P. C., Glover S. C. O., Klessen R. S., 2008, *ApJ*, 672, 757
- Clark P. C., Glover S. C. O., Smith R. J., Greif T. H., Klessen R. S., Bromm V., 2011, *Science*, 331, 1040
- Devecchi B., Volonteri M., 2009, *ApJ*, 694, 302
- Di Matteo T., Croft R. A. C., Feng Y., Waters D., Wilkins S., 2017, *MNRAS*, 467, 4243
- Dijkstra M., Haiman Z., Mesinger A., Wyithe J. S. B., 2008, *MNRAS*, 391, 1961
- Done C., Davis S. W., Jin C., Blaes O., Ward M., 2012, *MNRAS*, 420, 1848
- Done C., Gierliński M., Kubota A., 2007, *A&A Rev.*, 15, 1
- Druschke M., Schauer A. T. P., Glover S. C. O., Klessen R. S., 2020, *MNRAS*, 498, 4839
- Fan X. et al., 2006, *AJ*, 131, 1203
- Fernandez R., Bryan G. L., Haiman Z., Li M., 2014, *MNRAS*, 439, 3798
- Fragione G., Kocsis B., Rasio F. A., Silk J., 2022, *ApJ*, 927, 231
- Fuller T. M., Couchman H. M. P., 2000, *ApJ*, 544, 6
- González E., Kremer K., Chatterjee S., Fragione G., Rodriguez C. L., Weatherford N. C., Ye C. S., Rasio F. A., 2021, *ApJ*, 908, L29
- Haemmerlé L., Woods T. E., Klessen R. S., Heger A., Whalen D. J., 2018a, *ApJ*, 853, L3
- Haemmerlé L., Woods T. E., Klessen R. S., Heger A., Whalen D. J., 2018b, *MNRAS*, 474, 2757
- Hahn O., Abel T., 2011, *MNRAS*, 415, 2101
- Haiman Z., 2006, *New Astronomy Review*, 50, 672
- Hirano S., Hosokawa T., Yoshida N., Kuiper R., 2017, *Science*, 357, 1375
- Hirano S., Hosokawa T., Yoshida N., Umeda H., Omukai K., Chiaki G., Yorke H. W., 2014, *ApJ*, 781, 60
- Hopkins P. F., Cox T. J., Hernquist L., Narayanan D., Hayward C. C., Murray N., 2013, *MNRAS*, 430, 1901
- Hosokawa T., Omukai K., Yorke H. W., 2013, *ApJ*, 778, 178
- Hosokawa T., Yorke H. W., Inayoshi K., Omukai K., Yoshida N., 2013, *ApJ*, 778, 178
- Hosokawa T., Yorke H. W., Omukai K., 2010, *ApJ*, 721, 478
- Hunter J. D., 2007, *Computing in Science & Engineering*, 9, 90
- Inayoshi K., Haiman Z., Ostriker J. P., 2016a, *MNRAS*, 459, 3738
- Inayoshi K., Haiman Z., Ostriker J. P., 2016b, *MNRAS*, 459, 3738
- Jaura O., Glover S. C. O., Wollenberg K. M. J., Klessen R. S., Geen S., Haemmerlé L., 2022, *MNRAS*, 512, 116
- Jiang Y.-F., Stone J., Davis S. W., 2017, *ArXiv e-prints*
- Katz H., Sijacki D., Haehnelt M. G., 2015, *MNRAS*, 451, 2352
- Kim S. et al., 2009, *ApJ*, 695, 809
- Kitayama T., Yoshida N., Susa H., Umemura M., 2004, *ApJ*, 613, 631
- Kormendy J., Ho L. C., 2013, *ARA&A*, 51, 511
- Krumholz M. R., McKee C. F., Klein R. I., 2004, *ApJ*, 611, 399
- Kulkarni M., Visbal E., Bryan G. L., 2021, *ApJ*, 917, 40
- Latif M. A., Bovino S., Van Borm C., Grassi T., Schleicher D. R. G., Spaans M., 2014a, *MNRAS*, 443, 1979
- Latif M. A., Niemeyer J. C., Schleicher D. R. G., 2014, *MNRAS*, 440, 2969
- Latif M. A., Schleicher D. R. G., Bovino S., Grassi T., Spaans M., 2014b, *ApJ*, 792, 78
- Latif M. A., Schleicher D. R. G., Hartwig T., 2016, *MNRAS*, 458, 233
- Latif M. A., Whalen D. J., Khochfar S., Herrington N. P., Woods T. E., 2022, *Nature*, 607, 48
- Lupi A., Colpi M., Devecchi B., Galanti G., Volonteri M., 2014, *MNRAS*, 442, 3616
- Lupi A., Haardt F., Dotti M., Fiacconi D., Mayer L., Madau P., 2016, *MNRAS*, 456, 2993
- Lupi A., Haiman Z., Volonteri M., 2021, *MNRAS*, 503, 5046
- Machacek M. E., Bryan G. L., Abel T., 2001, *ApJ*, 548, 509
- Madau P., Rees M. J., 2001, *ApJ*, 551, L27
- Matsuoka Y. et al., 2019, *ApJ*, 883, 183
- Mayer L., Kazantzidis S., Escala A., Callegari S., 2010, *Nature*, 466, 1082
- Mazzucchelli C., Bañados E., Decarli R., Farina E. P., Venemans B. P., Walter F., Overzier R., 2017, *ApJ*, 834, 83
- Milosavljević M., Couch S. M., Bromm V., 2009, *ApJ*, 696, L146
- Murray S. G., Power C., Robotham A. S. G., 2013, *Astronomy and Computing*, 3, 23
- Natarajan P., 2020, *MNRAS*
- O'Shea B. W., Abel T., Whalen D., Norman M. L., 2005, *ApJ*, 628, L5
- Overzier R. A., 2022, *ApJ*, 926, 114
- Planck Collaboration et al., 2014, *A&A*, 571, A16
- Planck Collaboration et al., 2020, *A&A*, 641, A6
- Portegies Zwart S. F., Baumgardt H., Hut P., Makino J., McMillan S. L. W., 2004, *Nature*, 428, 724
- Press W. H., Schechter P., 1974, *ApJ*, 187, 425
- Prole L. R., Clark P. C., Klessen R. S., Glover S. C. O., 2022, *MNRAS*, 510, 4019
- Regan J. A., Downes T. P., 2018a, *MNRAS*, 475, 4636
- Regan J. A., Downes T. P., 2018b, *MNRAS*, 478, 5037
- Regan J. A., Downes T. P., Volonteri M., Beckmann R., Lupi A., Trebitsch M., Dubois Y., 2019, *MNRAS*, 486, 3892
- Regan J. A., Haehnelt M. G., 2009, *MNRAS*, 393, 858
- Regan J. A., Johansson P. H., Haehnelt M. G., 2014, *MNRAS*, 439, 1160
- Regan J. A., Johansson P. H., Wise J. H., 2016, *MNRAS*
- Regan J. A., Visbal E., Wise J. H., Haiman Z., Johansson P. H., Bryan G. L., 2017, *Nature Astronomy*, 1, 0075
- Regan J. A., Wise J. H., O'Shea B. W., Norman M. L., 2020a, *MNRAS*, 492, 3021
- Regan J. A., Wise J. H., Woods T. E., Downes T. P., O'Shea B. W., Norman M. L., 2020b, *The Open Journal of Astrophysics*, 3, 15
- Reines A. E., Condon J. J., Darling J., Greene J. E., 2020, *ApJ*, 888, 36
- Reinoso B., Klessen R. S., Schleicher D., Glover S. C. O., *Solar P.*, 2023, *MNRAS*
- Rizzuto F. P. et al., 2021, *MNRAS*, 501, 5257
- Sądowski A., 2009, *ApJS*, 183, 171
- Sądowski A., Narayan R., McKinney J. C., Tchekhovskoy A., 2014, *MNRAS*, 439, 503
- Schaerer D., 2002, *A&A*, 382, 28
- Schauer A. T. P., Glover S. C. O., Klessen R. S., Clark P., 2021, *MNRAS*, 507, 1775
- Schauer A. T. P., Regan J., Glover S. C. O., Klessen R. S., 2017, *MNRAS*, 471, 4878
- Schauer A. T. P., Whalen D. J., Glover S. C. O., Klessen R. S., 2015, *MNRAS*, 454, 2441
- Shang C., Bryan G. L., Haiman Z., 2010, *MNRAS*, 402, 1249
- Simpson C., Mortlock D., Warren S., Cantalupo S., Hewett P., McLure R., McMahon R., Venemans B., 2014, *MNRAS*, 442, 3454
- Skinner D., Wise J. H., 2020, *MNRAS*, 492, 4386
- Smith B. D. et al., 2017, *MNRAS*, 466, 2217
- Smith B. D., Regan J. A., Downes T. P., Norman M. L., O'Shea B. W., Wise J. H., 2018, *MNRAS*, 480, 3762
- Spinoso D., Bonoli S., Valiante R., Schneider R., Izquierdo-Villalba D., 2022, *arXiv e-prints*, arXiv:2203.13846

- Stacy A., Bromm V., 2014, *ApJ*, 785, 73
- Stone N. C., Küpper A. H. W., Ostriker J. P., 2017, *MNRAS*, 467, 4180
- Takeo E., Inayoshi K., Mineshige S., 2020, *MNRAS*, 497, 302
- Tanaka T. L., Li M., 2014, *MNRAS*, 439, 1092
- Tegmark M., Silk J., Rees M. J., Blanchard A., Abel T., Palla F., 1997, *ApJ*, 474, 1
- Trenti M., Stiavelli M., Shull J. M., 2009, *ApJ*, 700, 1672
- Tseliakhovich D., Hirata C., 2010, *Phys. Rev. D*, 82, 083520
- Turk M. J., Abel T., O’Shea B., 2009, *Science*, 325, 601
- Turk M. J., Oishi J. S., Abel T., Bryan G. L., 2012, *ApJ*, 745, 154
- Turk M. J., Smith B. D., Oishi J. S., Skory S., Skillman S. W., Abel T., Norman M. L., 2011, *ApJS*, 192, 9
- Venemans B. P. et al., 2015, *ApJ*, 801, L11
- Visbal E., Haiman Z., Bryan G. L., 2014a, *MNRAS*, 442, L100
- Visbal E., Haiman Z., Bryan G. L., 2014b, *MNRAS*, 445, 1056
- Visbal E., Haiman Z., Terrazas B., Bryan G. L., Barkana R., 2014, *ArXiv e-prints*
- Wang F. et al., 2021, *arXiv e-prints*, arXiv:2101.03179
- Willott C. J., Percival W. J., McLure R. J., Crampton D., Hutchings J. B., Jarvis M. J., Sawicki M., Simard L., 2005, *ApJ*, 626, 657
- Wise J. H., Abel T., 2011, *MNRAS*, 414, 3458
- Wise J. H., Demchenko V. G., Halicek M. T., Norman M. L., Turk M. J., Abel T., Smith B. D., 2014, *MNRAS*, 442, 2560
- Wise J. H., Regan J. A., O’Shea B. W., Norman M. L., Downes T. P., Xu H., 2019, *Nature*, 566, 85
- Wise J. H., Turk M. J., Norman M. L., Abel T., 2012, *ApJ*, 745, 50
- Wolcott-Green J., Haiman Z., 2019, *MNRAS*, 484, 2467
- Wolcott-Green J., Haiman Z., Bryan G. L., 2011, *MNRAS*, 418, 838
- Woods T. E. et al., 2019, *PASA*, 36, e027
- Woods T. E., Heger A., Whalen D. J., Haemmerlé L., Klessen R. S., 2017, *ApJ*, 842, L6
- Woods T. E., Willott C. J., Regan J. A., Wise J. H., Downes T. P., Norman M. L., O’Shea B. W., 2021, *ApJ*, 920, L22
- Yoshida N., Abel T., Hernquist L., Sugiyama N., 2003, *ApJ*, 592, 645
- Zubovas K., King A., 2021, *MNRAS*, 501, 4289

This paper was built using the Open Journal of Astrophysics \LaTeX template. The OJA is a journal which provides fast and easy peer review for new papers in the `astro-ph` section of the arXiv, making the reviewing process simpler for authors and referees alike. Learn more at <http://astro.theoj.org>.